








## RESEARCH ARTICLE

10.1029/2022JD037841

# Observational and Model Impact of Tonga Volcano Eruption on Schumann Resonance

### Key Points:

- Lightning activity over Tonga volcano is clearly visible in Schumann resonance (SR) worldwide
- Model of extremely low frequency propagation with World Wide Lightning Location Network detections as a source gives qualitative agreement with observed SR enhancement during Tonga eruption
- Lightning activity during peak of Tonga eruption is so high that it significantly suppresses global lightning detection rate

A. Mezentsev<sup>1</sup> , A. P. Nickolaenko<sup>2</sup> , A. V. Shvets<sup>2,3</sup>, Yu. P. Galuk<sup>4</sup>, A. Yu. Schekotov<sup>5</sup> , M. Hayakawa<sup>6,7</sup> , R. Romero<sup>8</sup> , J. Izutsu<sup>9</sup>, and I. G. Kudintseva<sup>10</sup>

<sup>1</sup>Birkeland Centre for Space Science, Department of Physics and Technology, University of Bergen, Bergen, Norway, <sup>2</sup>Usikov Institute for Radio-Physics and Electronics, National Academy of Sciences of Ukraine, Kharkov, Ukraine, <sup>3</sup>Research Center for Realizing Sustainable Societies, University of Electro-Communications, Tokyo, Japan, <sup>4</sup>Department of Applied Mathematics and Control Processes, Saint-Petersburg State University, Saint-Petersburg, Russia, <sup>5</sup>Institute of Physics of the Earth, Russian Academy of Sciences, Moscow, Russia, <sup>6</sup>Hayakawa Institute of Seismo Electromagnetics, University of Electro-Communications Alliance Center, Tokyo, Japan, <sup>7</sup>Advanced Wireless & Communications Research Center, University of Electro-Communications, Tokyo, Japan, <sup>8</sup>Independent Researcher, Cumiana, Italy, <sup>9</sup>International Digital Earth Applied Science Research Center, Chubu University, Kasugai, Japan, <sup>10</sup>Department of Mathematics and Informatics, Kharkov State University, Kharkov, Ukraine

### Correspondence to:

A. Mezentsev,  
[Andrey.Mezentsev@uib.no](mailto:Andrey.Mezentsev@uib.no)

### Citation:

Mezentsev, A., Nickolaenko, A. P., Shvets, A. V., Galuk, Y. P., Schekotov, A. Yu., Hayakawa, M., et al. (2023). Observational and model impact of Tonga volcano eruption on Schumann resonance. *Journal of Geophysical Research: Atmospheres*, 128, e2022JD037841. <https://doi.org/10.1029/2022JD037841>

Received 11 SEP 2022  
 Accepted 17 FEB 2023

### Author Contributions:

**Conceptualization:** A. P. Nickolaenko  
**Data curation:** A. Mezentsev, A. Yu. Schekotov, M. Hayakawa, R. Romero, J. Izutsu  
**Formal analysis:** A. Mezentsev, A. P. Nickolaenko, A. V. Shvets, Yu. P. Galuk, A. Yu. Schekotov, I. G. Kudintseva  
**Methodology:** A. P. Nickolaenko, A. V. Shvets, Yu. P. Galuk, A. Yu. Schekotov  
**Project Administration:** A. P. Nickolaenko  
**Resources:** A. Mezentsev  
**Software:** A. V. Shvets, Yu. P. Galuk, A. Yu. Schekotov  
**Validation:** A. Mezentsev  
**Visualization:** A. Mezentsev, A. V. Shvets

**Abstract** Tonga volcano eruption on 15 January 2022 was accompanied by an unprecedentedly high lightning activity in the volcano plume which significantly exceeded the lightning activity level of the whole globe. We compare model computations with the observed effect of the Tonga volcano eruption on the global electromagnetic Schumann resonance (SR). This SR disturbance was detected at many observatories covering the whole globe. SR power spectral density was computed using the updated model of the Earth-ionosphere cavity, with the global lightning detections recorded by the World Wide Lightning Location Network, as a source. The modeled dynamics of the SR disturbances during Tonga eruption agrees qualitatively and quantitatively with SR recordings from six globally separated observatories. Unprecedentedly high lightning activity during the active phase of eruption caused significant suppression of the global lightning detection rate without noticeable effect on real global thunderstorm activity.

**Plain Language Summary** Tonga volcano exploded 15 January 2022. This catastrophic event was accompanied by huge lightning activity in the vicinity of volcano inside quickly expanding volcanic plume. Lightning activity in that volcanic cloud was so high that for several hours it significantly overrode the lightning activity of the whole planet. The Earth-ionosphere cavity represents a spherical resonator where electromagnetic (EM) waves of extremely low frequencies can propagate and amplify their amplitude on certain resonant frequencies. This phenomenon is called Schumann resonance (SR). SR can be observed everywhere over the globe at any time due to permanent global lightning activity. During Tonga volcano eruption different globally separated SR observatories registered power increase in the SR band exceeding the normal planetary background level by an order of magnitude. This is extremely high for a point source represented by this volcano. We used a model of EM wave propagation in the Earth-ionosphere cavity and lightning detections recorded by World Wide Lightning Location Network (WWLLN) as source of EM waves to model the impact of the volcanic lightning activity on the global SR level. We analyzed the impact of extremely high lightning rate on the performance of WWLLN, which was significantly suppressed during active phase of eruption.

## 1. Introduction

Considerable progress has been achieved recently in monitoring and modeling the global electromagnetic (EM) Schumann resonance (SR). As a result, we are able to successfully interpret and simulate the observed resonance signals in the extremely low frequency (ELF) band, both in the frequency and in the time domain (Kudintseva et al., 2016; Nickolaenko et al., 2016; Nickolaenko & Hayakawa, 2002, 2014). For this purpose one must know the conductivity profile of the middle atmosphere, position of the observer, and the location of the field sources on the planet. We take advantage of this opportunity for simulating the impact from the volcanogenic lightning activity on the SR signals recorded at six ELF observatories positioned worldwide during the Hunga Tonga-Hunga Ha'apai (hereafter Tonga) volcano eruption on 15 January 2022.

© 2023 University of Bergen.  
 This is an open access article under the terms of the [Creative Commons Attribution License](https://creativecommons.org/licenses/by/4.0/), which permits use, distribution and reproduction in any medium, provided the original work is properly cited.

**Writing – original draft:** A. Mezentsev, A. P. Nickolaenko  
**Writing – review & editing:** A. Mezentsev, A. P. Nickolaenko, A. V. Shvets, Yu. P. Galuk, A. Yu. Schekotov, M. Hayakawa, R. Romero, J. Izutsu, I. G. Kudintseva

**Table 1**  
*ELF Observatories Characteristics*

Station acronym	Latitude, °N	Longitude, °E	Distance <sup>a</sup> , Mm	Azimuth <sup>b,c</sup> + $M_{decl}^b$ , °	Field recorded			Sampling frequency, Hz
					$B_{ew}$	$B_{ns}$	$E_z$	
KRM	52.94	158.13	8.53	154.54 + 7.26	+	+	–	100
NKG	35.42	137.55	7.94	133.56 + 7.98	+	+	–	100
CMN	44.96	7.42	17.28	6.27 <sup>d</sup>	–	–	+	224
GRN	44.19	0.02	17.35	–10.50 – 1.04	–	+ <sup>e</sup>	–	250
FCH	58.76	–94.08	11.45	–107.97 + 1.55	+	+	–	20
MST	53.35	–112.97	10.13	–123.73 – 13.81	+	+	–	20

<sup>a</sup>Great circle distance between the volcano and a station. <sup>b</sup>Azimuth from a station to the volcano measured clockwise from north. <sup>c</sup> $M_{decl}$  is magnetic declination at the station location, positive for declination to the west. <sup>d</sup>CMN station measures vertical electric field, so no need to know magnetic declination. <sup>e</sup>GRN station measures single horizontal magnetic field component oriented at 23° to the east.

Tonga volcano (20.54°S, 175.38°W) eruption on 15 January 2022 was accompanied by severe lightning activity in the rapidly expanding volcanic plume. This volcanogenic lightning activity produced strong disturbances in the SR band recorded by four globally separated ELF stations as reported by Nickolaenko et al. (2022). In this contribution we compare power spectral density (PSD) of SR recordings from six globally separated ELF observatories with modeled PSDs for those observatories.

As a source of EM radiation for SR modeling we use global lightning detection data from World Wide Lightning Location Network (WWLLN). WWLLN uses more than 70 very low frequency (VLF) receivers deployed over the globe to provide lightning detection, location and estimate of the stroke energy (see <http://wwlln.net>). Average accuracy of WWLLN detections is 5 km and 10 μs, and it varies significantly depending on the geographical location of the source discharge (Hutchins et al., 2012; Rodger et al., 2005). Accuracy for the energy estimation is quite poor, and cannot be assessed for a large part of the total amount of discharges. Nevertheless, we are using this energy information in our model calculations due to the lack of more reliable data.

## 2. ELF Observatories

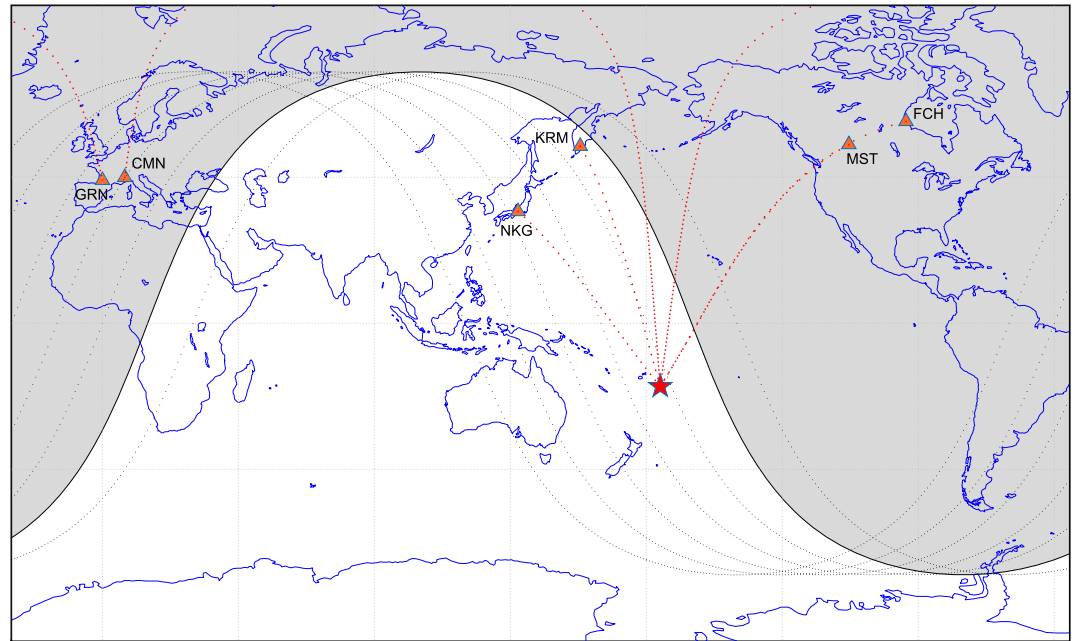
ELF data from six globally separated observatories were used for the analysis. Table 1 summarizes general characteristics of the six stations: Karimshino, KRM (Russia); Nakatsugawa, NKG (Japan); Cumiana, CMN (Italy); Lot et Garonne, GRN (France); Canadian Array for Realtime Investigations of Magnetic Activity (CARISMA) network sites FCHU, FCH, and MSTK, MST (Canada). Four of these observatories record both components of the horizontal magnetic field,  $B_{ew}$  and  $B_{ns}$  (east-west and north-south): KRM, NKG, FCH, MST. GRN station records only one magnetic component,  $B_{ns}$ , whose axis is oriented at 23° toward east from north. CMN observatory records vertical electric field,  $E_z$ . European and Asian observatories make their recordings at a sampling frequency high enough to pick spectral contents higher than 30 Hz (the upper limit of our focus range). Canadian network operates FCH and MST stations at 100 Hz sampling frequency, but publicly available data are down-sampled at 20 Hz (Mann et al., 2008), which limits the spectral contents of their data at upper level of 10 Hz, allowing us to analyze only the first SR peak. Other four stations (KRM, NKG, CMN, and GRN) can discern at least four first SR peaks.

Figure 1 shows mutual geographical positioning of the Tonga volcano and all six ELF observatories. Day-night terminator is shown for the peak hour of Tonga eruption, 05:00 UTC, 15 January 2022, with night side shaded by gray color. Great circle trackers (the shortest ones) between the volcano and all stations are marked by red dotted tracks.

## 3. Model Description

### 3.1. General Assumptions

We assume that the uniform Earth–ionosphere cavity is formed by a perfectly conducting spherical Earth surrounded by an atmosphere with certain conductivity profile. This allows us to describe EM wave propagation in the frequency



**Figure 1.** Location of Tonga volcano (red star) and six extremely low frequency observatories (orange triangles). Night side corresponding to 05:00 UTC 15 January 2022 is shaded by gray color. Red point trackers show great circle paths between the volcano and each observatory. Series of day-night terminator lines for 04:00 to 10:00 UTC with 1 hr step are shown as thin black dotted lines.

range from a few fractions of a hertz to a few kilohertz. Here we use a globally averaged vertical profile of mesospheric conductivity, ignoring the day–night difference. Earth–ionosphere cavity is supposed to be independent of the angular coordinates, which means that we neglect the effect of the geomagnetic field in our model.

We find the full-wave solution in the Earth–ionosphere cavity in the frequency range 3–30 Hz with 0.1 Hz frequency resolution. We derive the complex propagation constant of ELF radio waves  $\nu(f)$ . This propagation constant is then used to calculate the complex spectral components of the vertical electric field  $E_z$  and the transversal horizontal magnetic field  $B_\phi$  at the Earth surface for given observer and source locations.

As a source of ELF radiation we use WWLLN catalog with reported time, geolocation, and energy of the strokes. As a VLF system, WWLLN cannot be a good representation of the ELF emissions that are relevant for SR modeling. However, we assume here that because SR originates from global thunderstorm activity, WWLLN can give some general representation of the global EM radiation that will allow us to obtain results consistent with observational data.

### 3.2. Earth-Ionosphere Cavity

For calculating the realistic power spectra of SR signals, one has to introduce a credible model of the Earth–ionosphere cavity. We use a resonator model bounded by perfectly conducting spherical Earth surrounded by conducting atmosphere. The characteristics of cavity are independent of the angular coordinates. The air conductivity is characterized by the vertical conductivity profile  $\sigma(z)$ , it grows with altitude  $z$ , and the atmosphere gradually turns from essentially non-conducting into a perfectly conducting ionosphere at around 100 km altitude (Kudintseva et al., 2016). The particular conductivity profile  $\sigma(z)$  that we use in this work is taken from Nickolaenko et al. (2016).

We calculate the propagation parameters of ELF radio waves relevant to particular cavity model by using the full-wave solution (Galuk, 2016; Kudintseva et al., 2016; Nickolaenko et al., 2016; Nickolaenko et al., 2016a, 2016b). As a result, we get the complex propagation constant  $\nu(\omega)$ . Spectral densities of the field components radiated from a vertical point dipole source with a unit amplitude current moment  $m_1$  in the spherically symmetric uniform

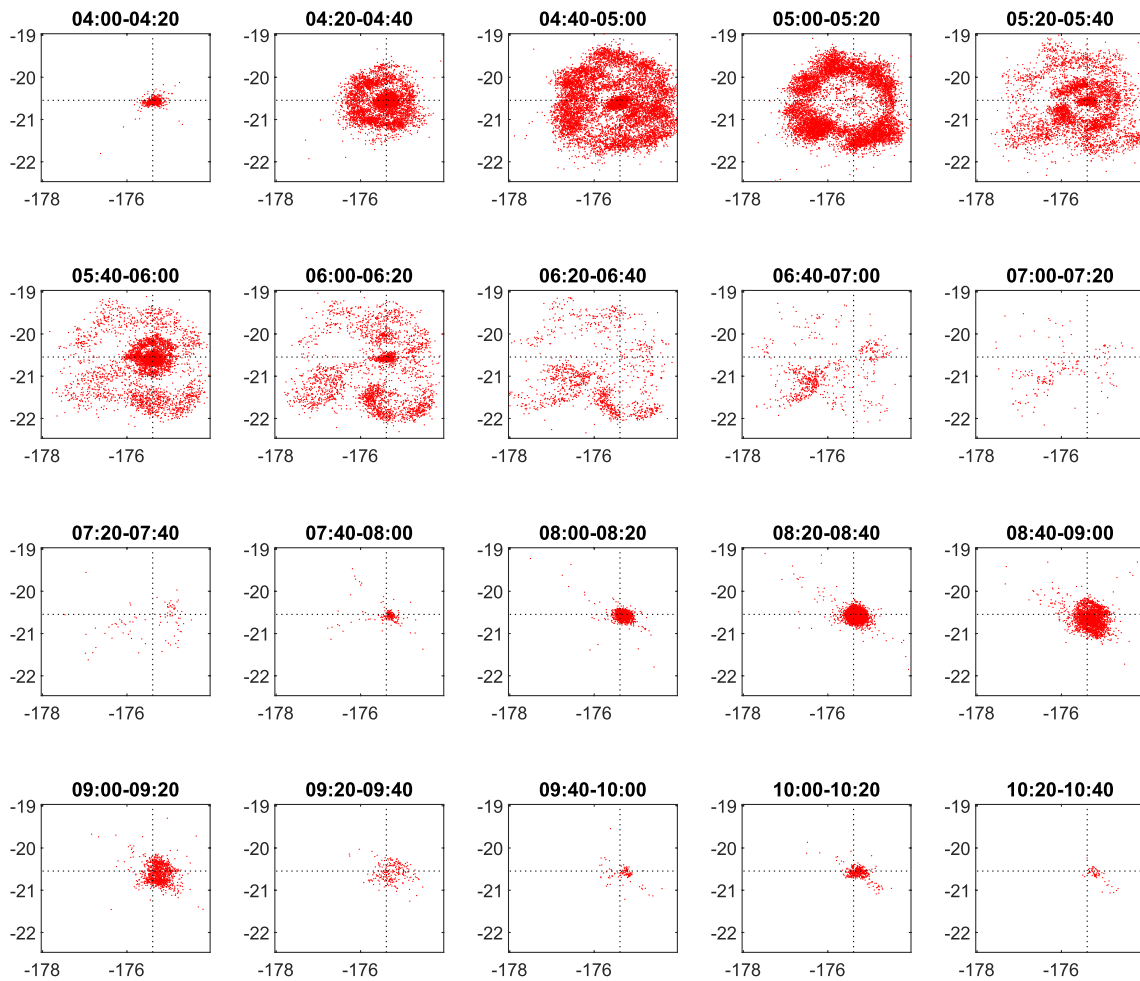


**Figure 2.** World Wide Lightning Location Network discharges dynamics around Tonga eruption. 20 min accumulation frames include all discharges within 300 km radius from the volcano.

Earth–ionosphere cavity are calculated using the following equations (Burke & Jones, 1996; Galuk, 2016; Jones, 1976; Nickolaenko & Hayakawa, 2002, 2014):

$$e_z = m_1 \frac{i}{4a^2 \omega \epsilon_0 N_0} \nu(\nu + 1) \frac{P_\nu^0(-\cos \theta)}{\sin \pi \nu}, \quad (1)$$

$$h_\phi = -m_1 \frac{1}{4aN_0} \frac{P_\nu^1(-\cos \theta)}{\sin \pi \nu}. \quad (2)$$

Here  $e_z$  is the spectral density of the vertical electric field,  $h_\phi$  is the spectral density of the transversal horizontal magnetic field component (orthogonal to the source–observer great circle arc),  $m_1$  is the current moment of a unit amplitude,  $a$  is the Earth's radius,  $\omega$  is the circular frequency,  $\epsilon_0$  is the dielectric constant of the free space,  $N_0$  is the field norm which is close to the electric characteristic altitude of the conductivity profile, taken to be equal to 60 km in this model,  $\theta$  is the angular great circle source–observer distance,  $P_\nu^0$  and  $P_\nu^1$  are the Legendre and the associated Legendre functions of complex index (Galuk, 2016), and  $\nu(\omega)$  is the complex wave propagation constant, which is the zero-order mode eigenvalue of the Earth–ionosphere spherical cavity.

As we are discussing the impact on SR from lightning activity associated with Tonga eruption, it is suitable to consider transversal and longitudinal components of the magnetic fields, relative to Tonga–observer great circle arc. To do that we have to switch from the recorded  $B_{ew}$  and  $B_{ns}$  magnetic field components to  $B_{\phi_0}$  and  $B_{r_0}$ , which represent transversal (across) and longitudinal (along) components relative to the Tonga–observer great circle arc:

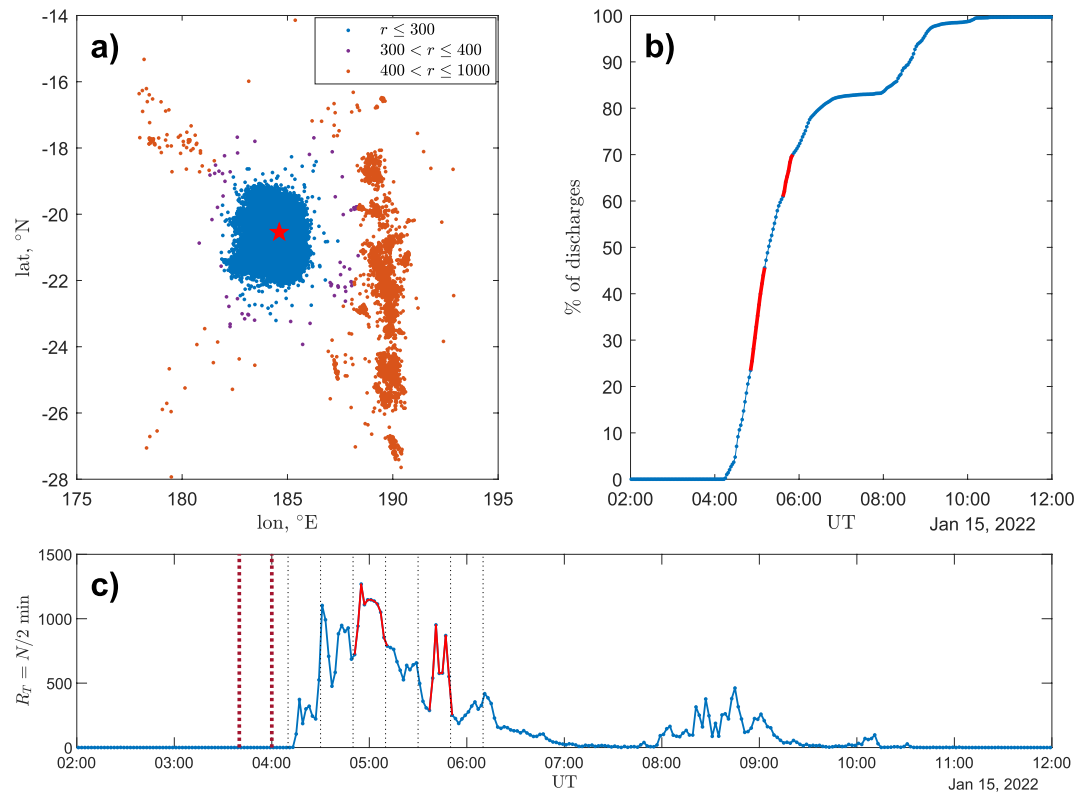


**Figure 3.** Panel (a): World Wide Lightning Location Network (WWLLN) discharges at different distances from Tonga volcano. Panel (b): cumulative distribution of number of lightning discharges around Tonga. Red segments highlight high peaks of activity. Panel (c): 2 min flash rate  $R_T$  dynamics of WWLLN discharges around Tonga. Red segments highlight high peaks of activity. Vertical dotted lines mark 20 min periods used for energy survey.

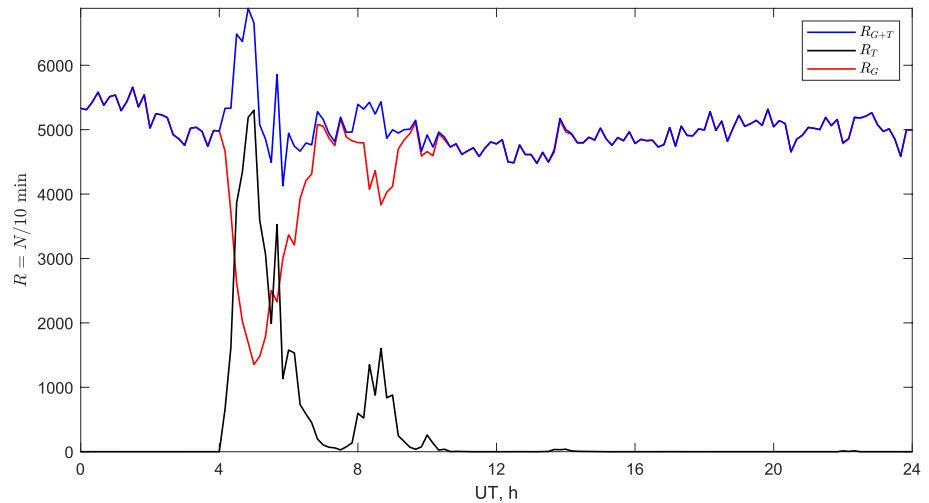


**Figure 4.** 10 minutes global combined flash rate  $R_{G+T}$  of World Wide Lightning Location Network (WWLLN) strokes (blue line). Black line shows flash rate  $R_T$  of WWLLN strokes detected within 300 km radius around Tonga. Red line shows global flash rate  $R_G$  with subtracted activity around Tonga volcano; it characterizes the “pure” planetary thunderstorm activity without considering Tonga associated discharges.

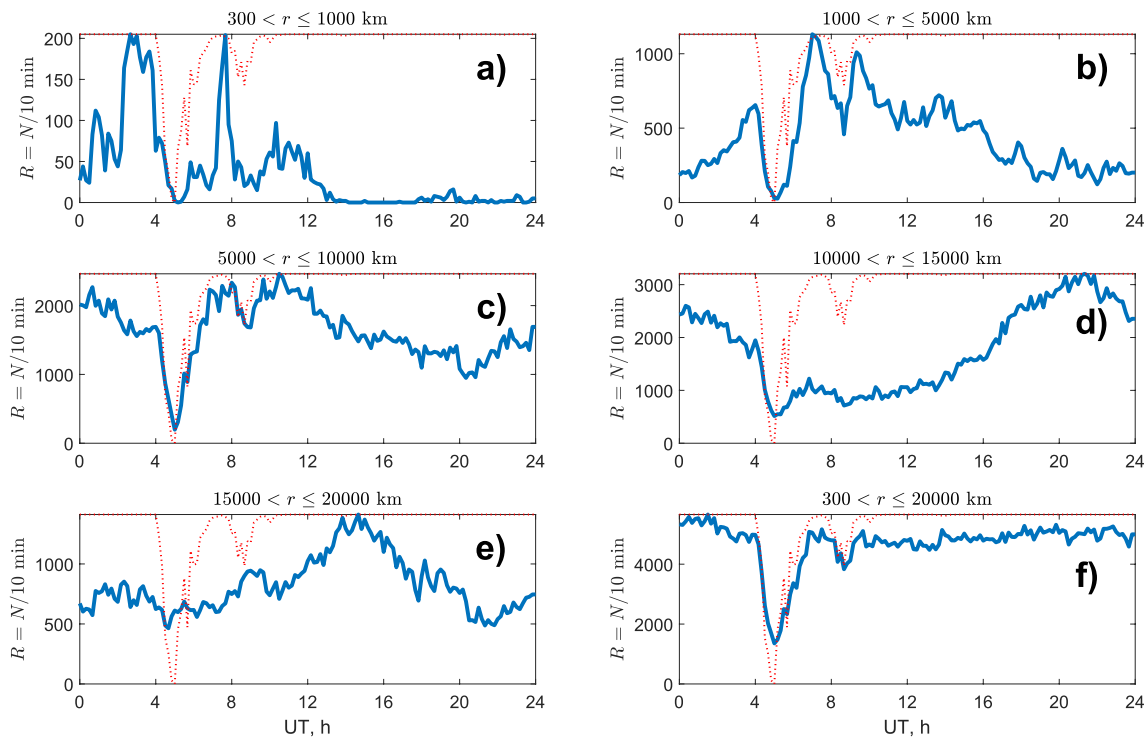


**Figure 5.** 10 minute flash rates  $R$  of World Wide Lightning Location Network (WWLLN) strokes detected within concentric rings of radius  $r$  around Tonga volcano (thick blue solid lines). For convenience normalized flash rate  $R_T$  of WWLLN strokes detected within 300 km radius around the volcano is shown upside-down plotted from the upper boundary (thin red dotted lines), to illustrate correlation between the flash rate  $R_T$  around Tonga and the dip in the flash rate at the rest of the globe.

$$\begin{aligned} B_{r_0} &= B_{ew} \sin \alpha_0 + B_{ns} \cos \alpha_0 \\ B_{\varphi_0} &= B_{ew} \cos \alpha_0 - B_{ns} \sin \alpha_0, \end{aligned} \quad (3)$$

where  $\alpha_0$  is the azimuth from an observational site to the Tonga volcano, accounting for the value of magnetic declination, see Table 1.

Similar technique can be used for modeled data. Transversal and longitudinal spectral components  $H_{\varphi_0}$  and  $H_{r_0}$  of modeled magnetic field can be found as a sum of individual spectral contributions from each source pulse:

$$\begin{aligned} H_{r_0}^2 &= \frac{1}{C} \sum_k |h_{\varphi_k}|^2 W_k \sin^2(\alpha_k - \alpha_0) \\ H_{\varphi_0}^2 &= \frac{1}{C} \sum_k |h_{\varphi_k}|^2 W_k \cos^2(\alpha_k - \alpha_0), \end{aligned} \quad (4)$$

where  $h_{\varphi_k}$  is the spectral density of the horizontal magnetic field component transversal to the observer–source direction for the  $k$ th field source (WWLLN stroke), see Equation 2,  $W_k$  is the energy of the  $k$ th stroke reported by WWLLN,  $\alpha_k$  and  $\alpha_0$  are azimuths from the observational site toward  $k$ th source and Tonga volcano correspondingly, and  $C$  is the normalization constant with dimension of energy, to make a stroke energy amplitude dimensionless, here we take  $C = 1$  J, as WWLLN reports energy in Joules. Summation goes along all sources within the time interval used to create modeled spectra.

Similarly, for the modeled spectral density of the vertical electric field during a certain time interval, we get:

$$E_z^2 = \frac{1}{C} \sum_k |e_{z_k}|^2 W_k, \quad (5)$$

where  $e_{z_k}$  is the spectral density of the vertical electric field created by the  $k$ th source, see Equation 1,  $C = 1$  J is the same normalization constant, and  $W_k$  is the energy of the  $k$ th stroke reported by WWLLN.



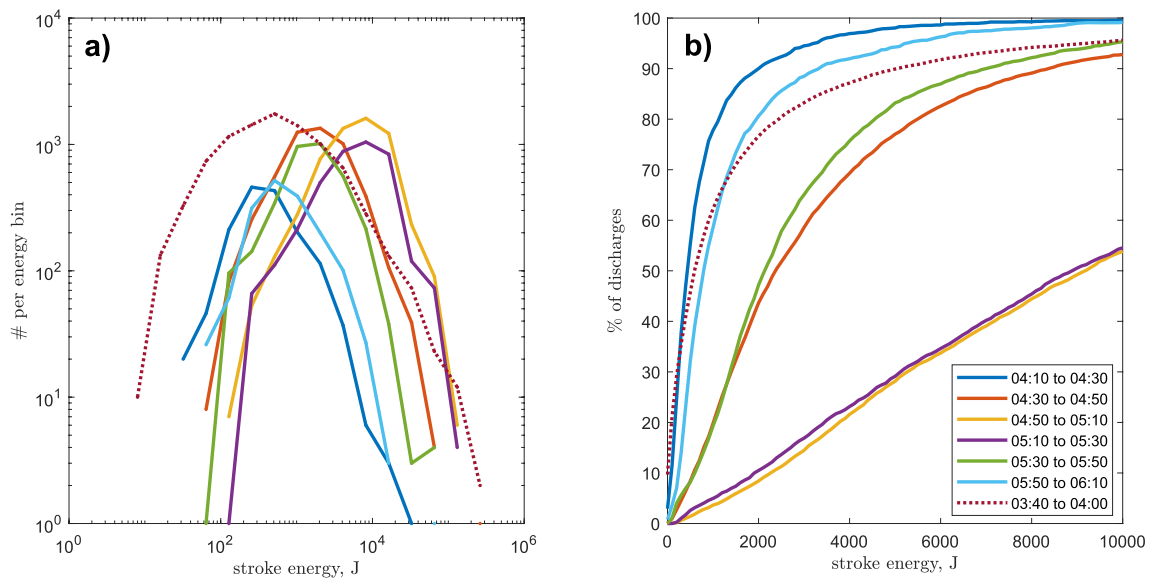


**Figure 6.** Panel (a): energy distributions for 20 min periods of the first main phase of Tonga related lightning activity (solid curves). Dotted curve represents a reference energy distribution of global lightning activity for quiet 20 min period just before the eruption. Panel (b): cumulative distributions of number of strokes over stroke energy for the same time intervals as in panel (a).

### 3.3. EM Field Sources

As EM field sources we use the WWLLN catalog of lightning detections, which provides occurrence time, geographical location, and energy estimate of lightning strokes worldwide. A series of strong assumptions must be made for using WWLLN catalog as EM source for our modeling.

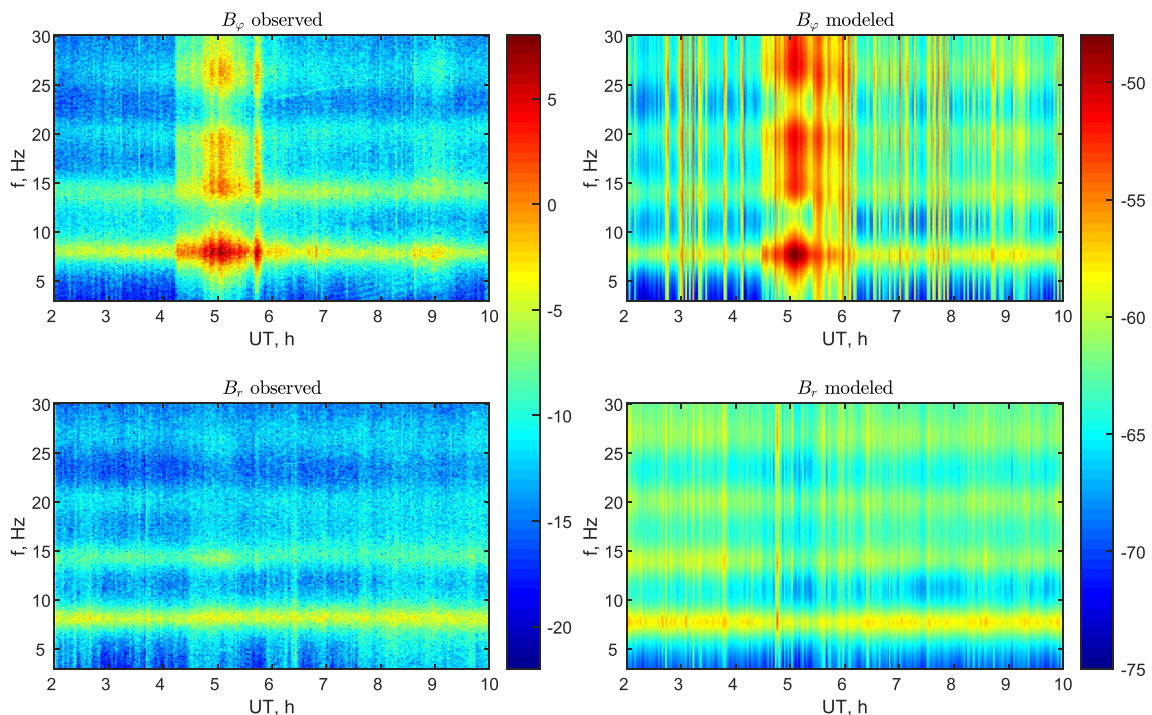


**Figure 7.** Power spectral density spectrograms for Karimshino station for observed (left panels) and modeled (right panels) transversal  $B_\phi$  (upper panels) and longitudinal  $B_r$  (lower panels) components of magnetic field. Color bars are in dB units.

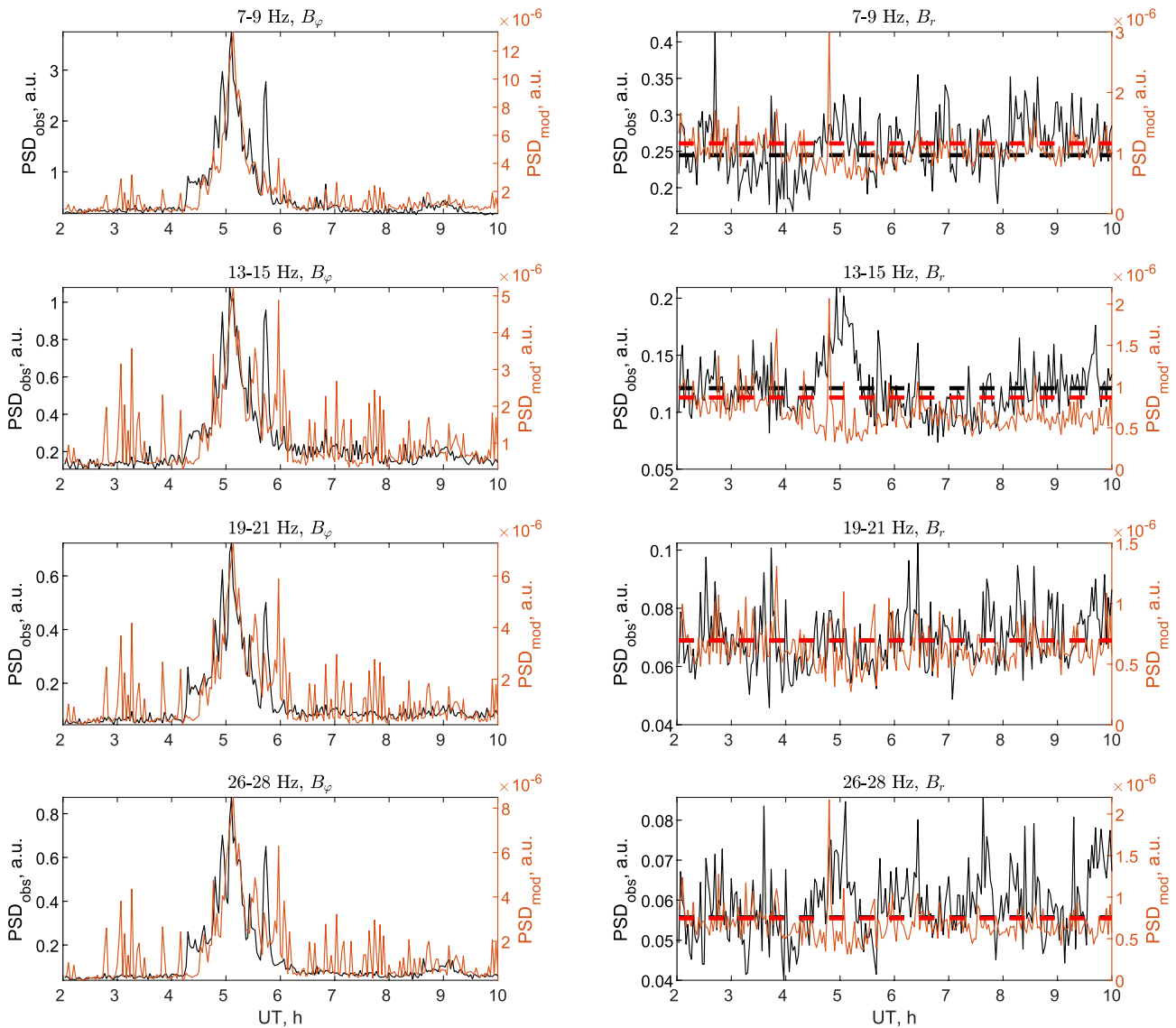


**Figure 8.** Averaged power spectral density along the first four Schumann resonance peaks for Karimshino station for observed (left axes) and modeled (right axes) transversal  $B_\phi$  (left panels) and longitudinal  $B_r$  (right panels) components of horizontal magnetic field.

First, we assume that radiation from the global thunderstorms detected by WWLLN in the 6–18 kHz range extends into the SR band. In particular, we suggest that the emission spectrum of all WWLLN discharges is “white,” that is, the source radiation is independent of the frequency. Obviously, such a strong assumption cannot be correct, and VLF representation of the global thunderstorm is not the same as ELF representation of it. However, we assume that we can use this representation as a first order approximation.

Second assumption relates to the reported energy of the strokes. Here we assume that PSD amplitudes of individual sources at SR frequencies are proportional to the energies  $W_k$  of those sources reported by WWLLN (see Equations 4 and 5).

Third, we assume that WWLLN detections form a Poissonian process, that is, lightning strokes are independent. This assumption allows us to consider PSD of the SR signal accumulated during a certain time interval as an additive sum of spectral powers of individual lightning strokes detected during this time interval. Such an assumption is commonly used in SR modeling (Kudintseva et al., 2017a, 2017b; Nikolaenko & Hayakawa, 2002; Shvets, 2001; Shvets et al., 2010). Thus, this last assumption allows us to ignore reported times of WWLLN



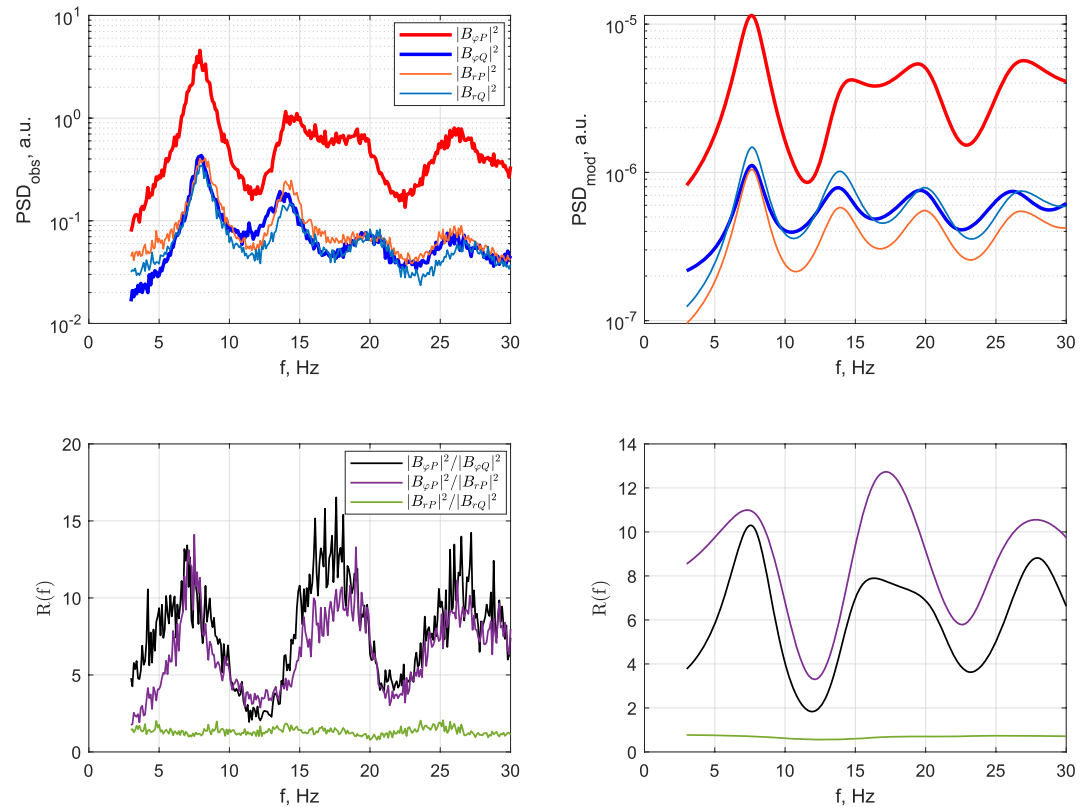


**Figure 9.** Characteristics of Schumann resonance power spectral density for observed (left panels) and modeled (right panels) data during peak period of eruption (04:50–05:10 UT) and quiet period (03:40–04:00 UT) at Karimshino observatory. Upper panels show spectral curves for  $B_\phi$  and  $B_r$  during peak period (red and orange curves), and for  $B_\phi$  and  $B_r$  during quiet period (blue and cyan curves). Lower panels characterize relative power increase in  $B_\phi$  component during peak period compared to quiet period (black curve);  $B_\phi$  over  $B_r$  component during peak period (purple curve); and  $B_r$  component during peak period compared to quiet period (green curve).

detections and to address modeled spectral densities in the additive form by using Equations 4 and 5 to calculate them based on WLLN data.

We should emphasize that obtaining the SR power spectrum produced in the Earth-ionosphere cavity by a vertical lightning discharge is not a problem. The problem is in introducing the realistic distribution of lightning discharges over the globe in time, relevant for ELF range. In this work we use WLLN data as field sources for our model. One can also exploit the data from optical spaceborne lightning monitoring instruments as field sources for SR modeling (Füllekrug, 2021).

#### 4. Lightning Activity Dynamics Accompanying Tonga Eruption

Tonga eruption produced an unprecedentedly high lightning activity in the volcanic plume. After the initial event, followed by a series of explosions (Astafyeva et al., 2022; Matoza et al., 2022; Wright et al., 2022), lightning activity was accompanying the eruption process for more than 6 hr. Spatial development of the discharges map during the active eruption phase is shown in Figure 2. Each frame in Figure 2 shows all WLLN detections within a radius of 300 km around the volcano during a 20 min accumulation period. A succession of central explosions ejecting ashes and hot water vapor into the atmosphere can be clearly tracked with rapidly expanding rings of lightning activity. We have to clarify that Figure 2 represents lightning activity in the volcanic plume, and not the seismic or volcanic activity themselves. Although, volcanic explosions produced new ejections into the atmosphere, which led to intensification of the lightning activity. This coupling between volcanic and EM activity deserves a dedicated study, but is outside the scope of this work.

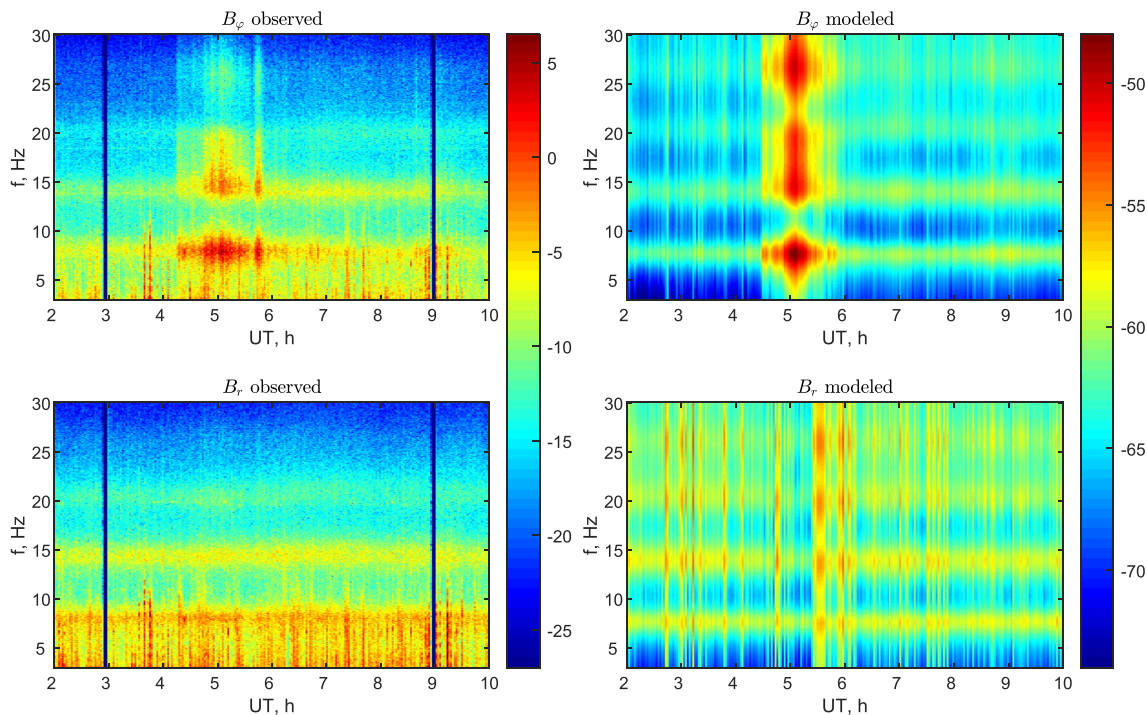


**Figure 10.** Power spectral density spectrograms for Nakatsugawa station for observed (left panels) and modeled (right panels) transversal  $B_{\phi}$  (upper panels) and longitudinal  $B_{\parallel}$  (lower panels) components of magnetic field. Color bars are in dB units.

The closest to Tonga planetary thunderstorm was at range 400–1,000 km east-southeast. Figure 3a shows all lightning detections during January 15 within 1,000 km around Tonga. Blue dots represents all strokes within 300 km radius. It is clearly seen that all eruption associated discharges are confined mainly within a circle of 200 km radius, with some extension at southwest up to 300 km. The closest atmospheric thunderstorm is shown by orange dots as longitudinally elongated cluster east from Tonga. This thunderstorm developed in a distance range 400–1,000 km from Tonga. This allows us to easily subtract Tonga eruption associated lightning activity from global thunderstorms. We selected all WWLLN detections within 300 km radius around Tonga, which guarantees getting all Tonga related activity, and safely preserves the global lightning activity of being affected by our selection.

Figure 3c shows 2 min flash rate  $R_T$  of WWLLN strokes within 300 km radius around Tonga between 02:00 and 12:00 UT. Volcano associated lightning activity starts at 04:15 UT and continues for about 6 hr, with two main phases: 04:15 to 07:00 UT, and 08:00 to 09:30 UT. The first phase was longer, more powerful and spatially extended (see Figure 2), with 3 times higher flash rate compared to the second phase. There was also the third phase, 10:00 to 10:30 UT, but its activity was quite small, so we do not consider it here.

The highest peak of activity in the first phase was between 04:50 and 05:10 UT. During those 20 min, according to the WWLLN recordings, 22% of total amount of Tonga associated discharges were released. Another remarkable peak of activity occurred between 05:36 and 05:50 UT, during those 14 min about 9% of discharges were released. These two sections of activity are highlighted with red on the flash rate curve (Figure 3c) and on the cumulative distribution of number of strokes (Figure 3b). Lightning activity dynamics can also be assessed by the cumulative distribution of the amount of WWLLN detections versus time (Figure 3b).

While trying to relate the Tonga associated lightning activity with global thunderstorm activity we realized that at its peak Tonga related flash rate reaches values of the global flash rate taken before the eruption. This shows that Tonga lightning generator was at least comparable (but we show below that it was more powerful) with the total planetary lightning activity. In Figure 4 we compare combined global 10 min flash rate  $R_{G+T}$ , considering all WWLLN detections, planetary plus Tonga related lightning (blue curve), Tonga associated 10 min flash rate  $R_T$ , with all strokes within 300 km radius circle around Tonga volcano (black curve), and the “pure” global planetary

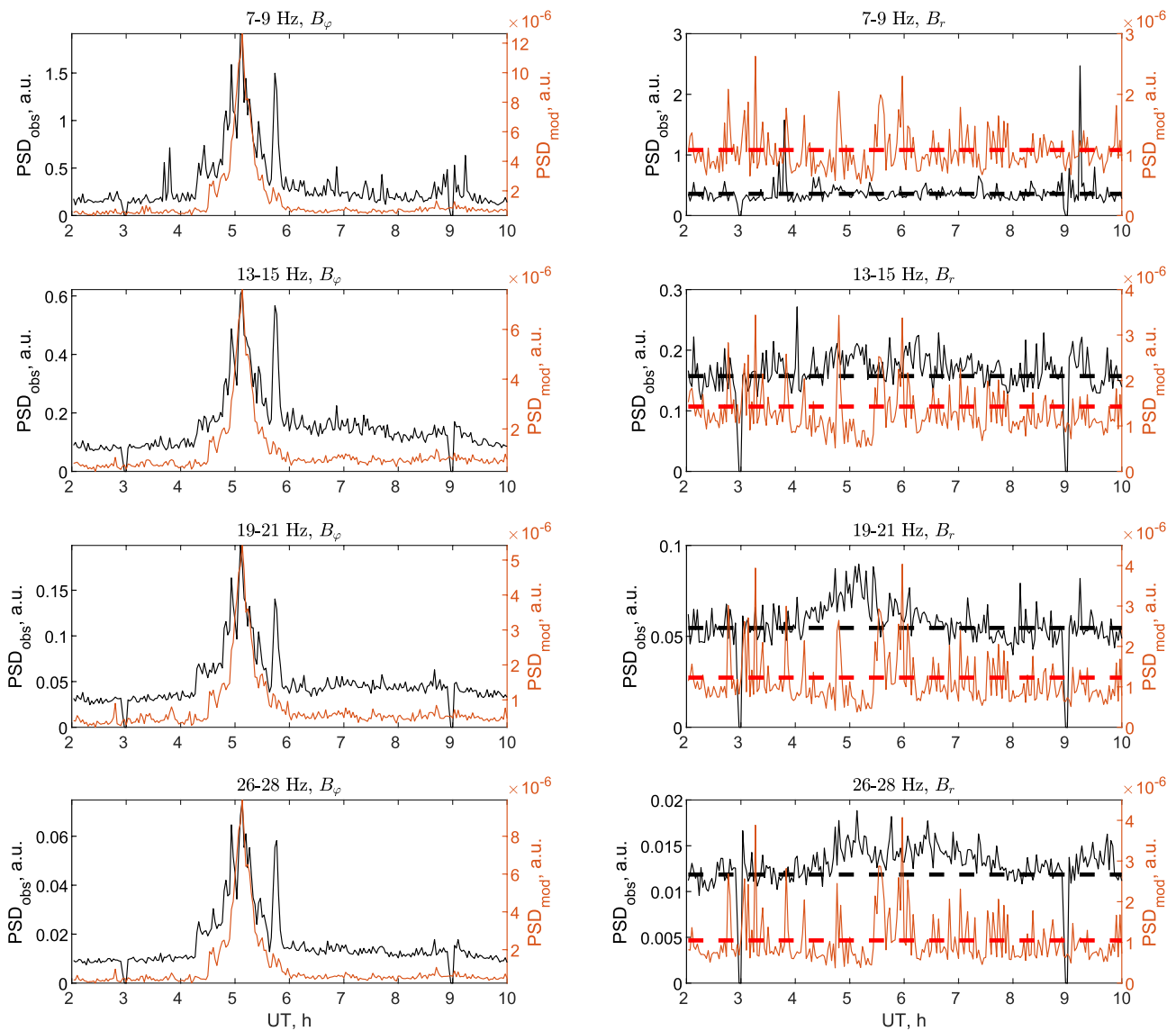


**Figure 11.** Averaged power spectral density along first four Schumann resonance peaks for Nakatsugawa station for observed (left axes) and modeled (right axes) transversal  $B_\phi$  (left panels) and longitudinal  $B_r$  (right panels) components of horizontal magnetic field.

10 min flash rate  $R_G$ , which shows only planetary lightning activity without volcano related discharges, which are totally alien to them (red curve).

We can see from Figure 4 that during lightning activity associated with Tonga eruption the combined global flash rate  $R_{G+T}$  does not show any particularly high increase (blue curve), whereas Tonga associated activity  $R_T$  reaches very high values (black curve). This means that during active eruption phase WWLLN experienced significant decrease in detection efficiency worldwide. If we consider only “pure” planetary lightning activity (non-related to the volcano), we can see a significant depletion in its flash rate  $R_G$  (red curve).

This detection efficiency decrease is distance dependent: the closer to the extreme concentration of strokes (the volcano), the more WWLLN detection efficiency decreases. In Figure 5 we present 10 min flash rates  $R$  calculated for strokes collected from concentric rings of different size around Tonga volcano: panels (a) to (e) show rings 300–1,000 km, 1,000–5,000 km, 5–10 Mm, 10–15 Mm, and 15–20 Mm. Panel (f) the whole planetary flash rate  $R_G$  without Tonga associated activity. Thin red dotted lines plotted upside-down from the upper boundary of each panel serves for guidance, to illustrate better the correlation between the dip in WWLLN flash rate  $R$  and the

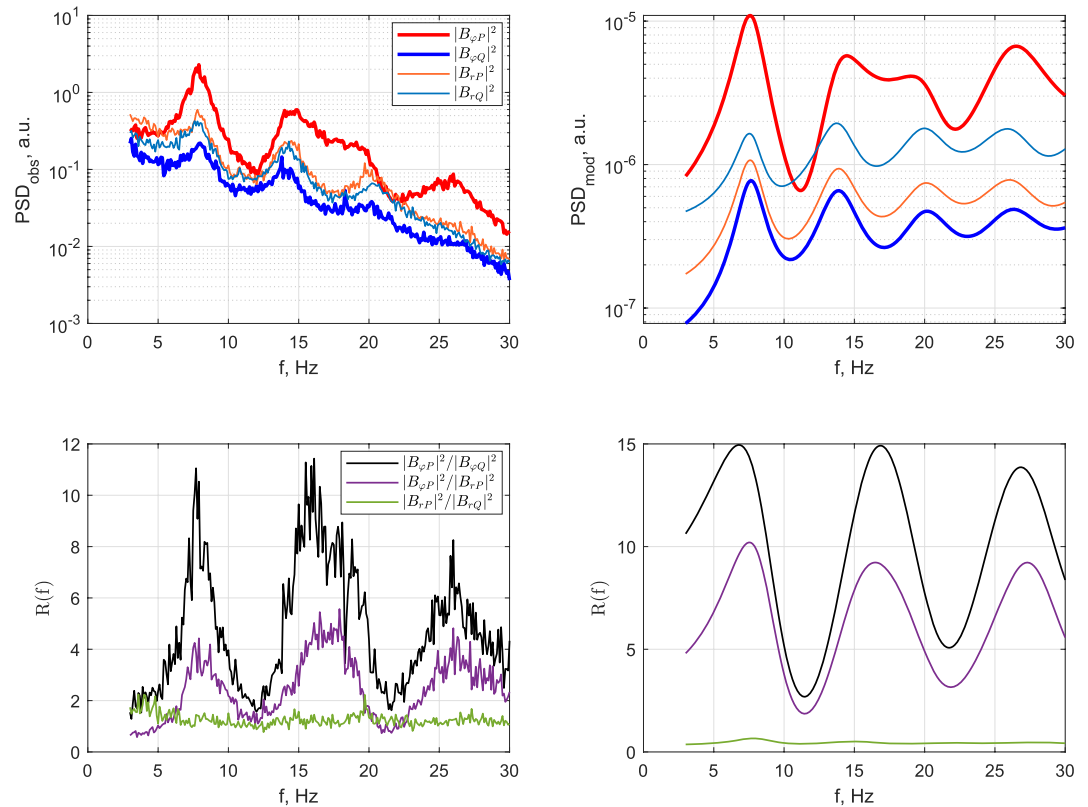


**Figure 12.** Characteristics of Schumann resonance power spectral density for observed and modeled data during eruption (04:50–05:10 UT) and quiet periods (03:02–03:22 UT) at Nakatsugawa observatory.

Tonga associated flash rate  $R_T$ . Panels (a) and (b) show that during the peak activity around Tonga detection rate within 5,000 km around Tonga drops practically down to zero. Even between 5 and 10 Mm detection rate drops to down to 10% level of its pre-eruption value (Figure 5c). 10–15 Mm ring experiences decrease down to 30% of its initial value (Figure 5d). Only between 15 and 20 Mm the dip in WWLLN detection rate cannot be distinguished. Panels (a) to (e) (distances up to 15 Mm) show dips in WWLLN flash rate well correlated with both main phases of Tonga associated lightning activity.

There can be two principal possible explanations for this dip in WWLLN detections:

1. dip in WWLLN detections is physical;
2. dip in WWLLN detections is instrumental.

First, “physical” possibility would mean that volcano related lightning activity somehow affected real thunderstorms around the planet, so they were producing less lightning discharges during the eruption. This scenario can be immediately rejected, as all types of EM monitoring data (including SR data presented below) do not support this possibility, demonstrating that planetary lightning activity level did not experience any reduction during the active phase of Tonga eruption (see the next Section).

Another possible physical cause that could lead to reduction of WWLLN detection efficiency is the effect that Tonga eruption put on the ionosphere. It has been reported that volcanic plume produced a giant long lasting hole in the ionosphere, reducing total electron content (TEC) significantly for several hours (Astafyeva et al., 2022). This TEC reduction could affect VLF propagation and reduce WWLLN efficiency, as WWLLN receives VLF lightning signal propagating in the Earth-ionosphere waveguide. In this scenario the real lightning flash rate is not affected by the volcano, but VLF wave propagation is disturbed because of TEC reduction, which leads to decreasing of WWLLN detection efficiency. This scenario can also be rejected, because during the peak phase of Tonga eruption nearly all WWLLN detections came from around volcano, where the ionosphere experienced the highest TEC reduction, and should have disturbed the VLF propagation in a more severe way than anywhere else.



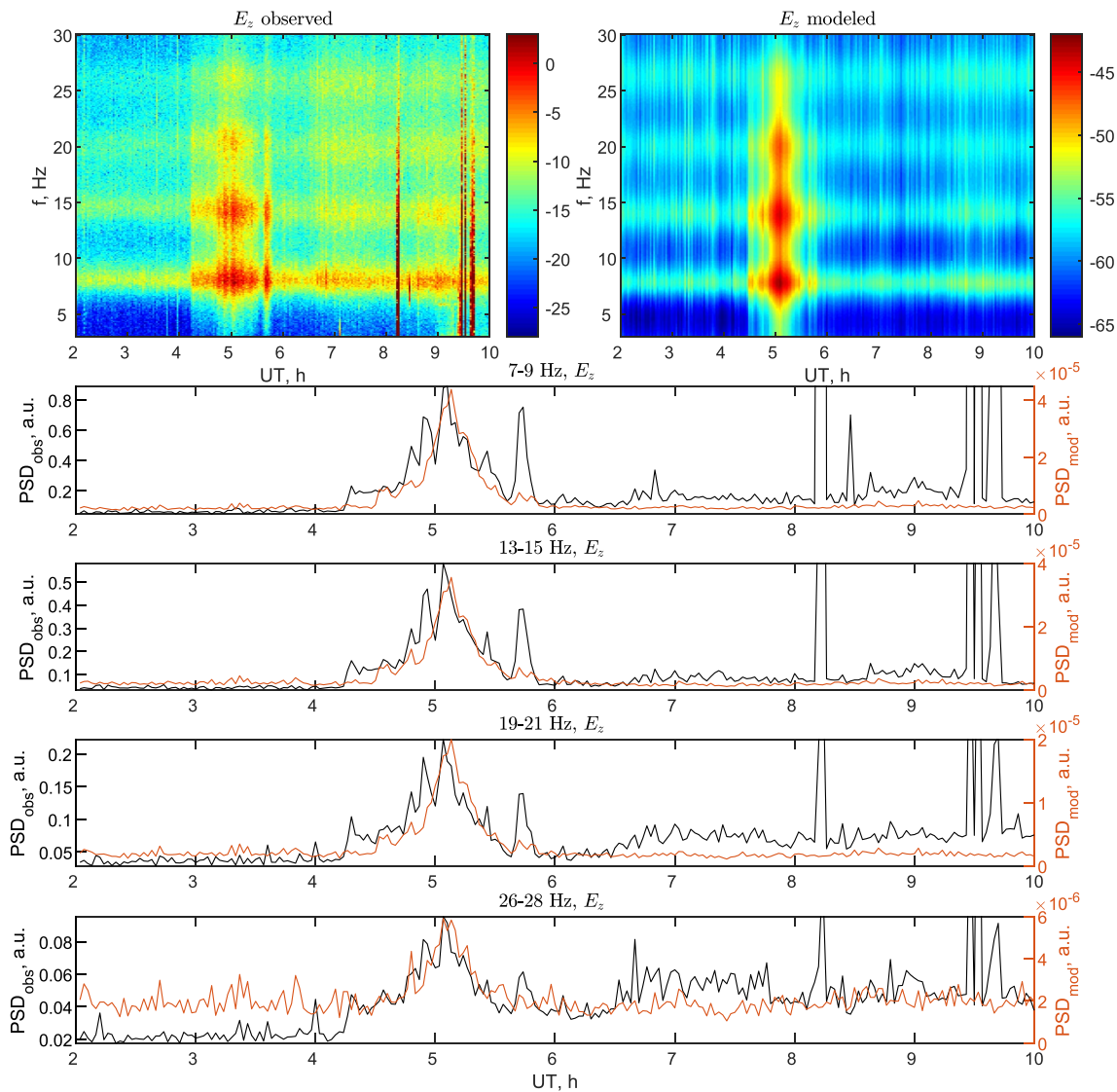


**Figure 13.** Power spectral density (PSD) spectrograms and averaged PSD along first four Schumann resonance peaks for Cumiana station for observed (left spectrogram) and modeled (right spectrogram) vertical electric field component.

Instrumental scenario means that WWLLN reduced its detection efficiency due to extremely high flash rate above the volcano during the peak phase of eruption. We find this scenario to be the most plausible. WWLLN uses flash rate dependent triggering threshold (Jacobson et al., 2006; Rodger et al., 2004): reaching high values of flash rate leads to increasing of triggering threshold to keep the global trigger rate to be around 8–10 triggers per second (in 2006 it was reported to be 5 triggers per second, but recent data demonstrate that WWLLN now operates at higher trigger rates). For example, during high flash rate periods only waveforms above certain amplitude level can generate a trigger. When the flash rate goes down, triggering threshold returns to its initial lower value.

Having an adaptive triggering threshold is an efficient way for keeping the flash rate below certain level when processing resources are limited. In general, when number of strokes increases drastically and overwhelms the system, the system sets a higher energy threshold and starts rejecting events with lower energies. Given the energy distribution of strokes, with most of the strokes being at lower energies (see Figure 6a), this turns to be a logical and effective way to solve the problem.

Figure 6a shows a survey of energy distribution of WWLLN strokes for different 20 min segments of Tonga related lightning activity (solid curves). As a reference we show energy distribution of global WWLLN activity for 20 min segment just before the eruption (reddish dotted curve). This reference segment, 03:40 to 04:00 UT, is



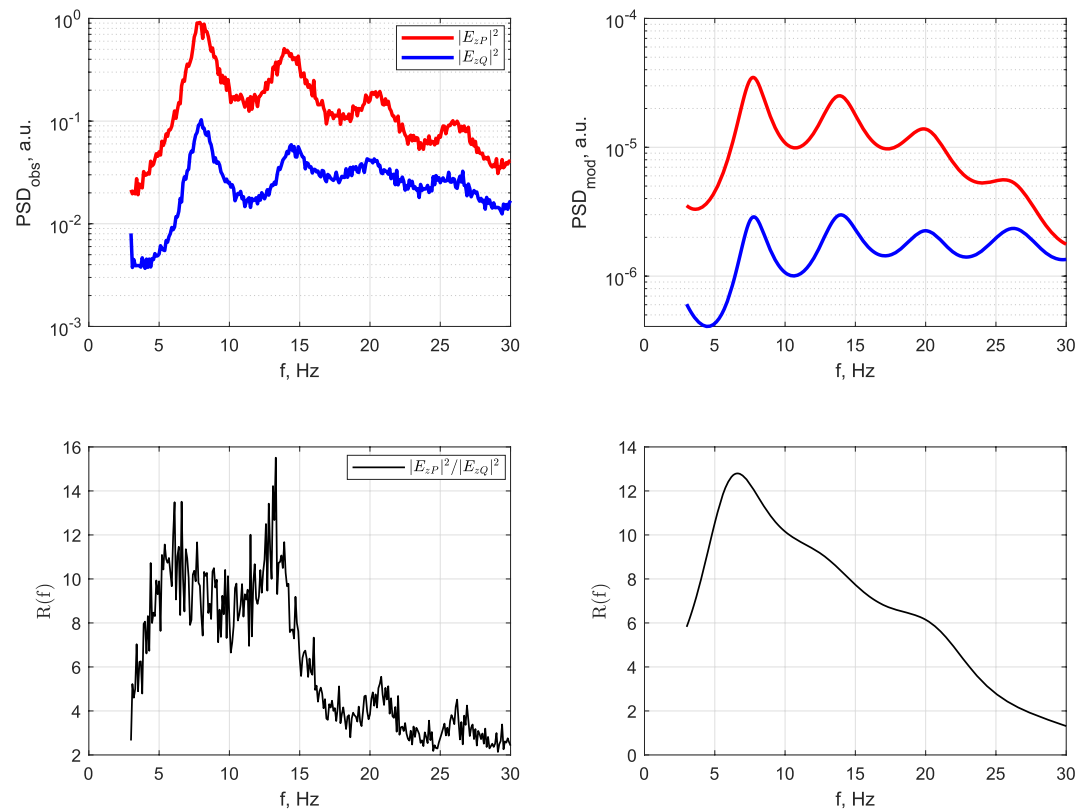


**Figure 14.** Characteristics of Schumann resonance power spectral density for observed and modeled data during eruption (04:50–05:10 UT) and quiet periods (03:02–03:22 UT) at Cumiana observatory.

a good choice, because global lightning activity level stayed constant between 02:00 and 04:00 UT; also because during the peak phase of eruption the amount of WWLLN detected strokes around Tonga is comparable with the amount of strokes detected globally during that 20 min quiet period. All these 20 min periods of the energy survey are marked with vertical dotted lines in Figure 3c.

While Tonga flash rate  $R_T$  grows higher, energy distribution experiences significant shift toward higher energies (Figure 6a), which is equivalent to effective cutting off of about 90% of total physical discharges (Figure 6b). In Figure 6b we show cumulative distribution of number of strokes with certain energies, calculated for the same 20 min segments shown in Figure 6a. We can see that during the low level of activity and during reference quiet period the main contribution to the total amount of discharges is made in lower energies: first and last segments of Tonga related activity (04:10 to 04:30, and 05:50 to 06:10 UT), and the reference quiet period have 90% of their discharges concentrated among energies below 2, 3, and 5 kJ correspondingly. Whereas periods of highest Tonga related activity have only 10%, 15%, and 30% of their strokes below those energy levels correspondingly (Figure 6b). This fact does not mean that overall energy distribution of Tonga related discharges moved toward higher energies. The character of distribution most probably stayed the same, but WWLLN only registered the high energy tail from the total amount of physical discharges. This area deserves a separate dedicated study, and we will not address it here.

## 5. Observational and Modeling Results

Here we present SR dynamic spectrograms for the six ELF stations: KRM, NKG, CMN, GRN, FCH, and MST, focusing on comparing the observed and modeled PSDs. Four stations that monitor both horizontal magnetic field components (KRM, NKG, FCH, MST) allow for switching to transversal and longitudinal magnetic field components, see Equations 3 and 4, relative to the direction toward the Tonga volcano, both for observed and modeled spectra. GRN station monitors only  $B_{ns}$  magnetic field component, and does not allow for the field rotation. CMN station records vertical electric field  $E_z$ , which is omnidirectional.

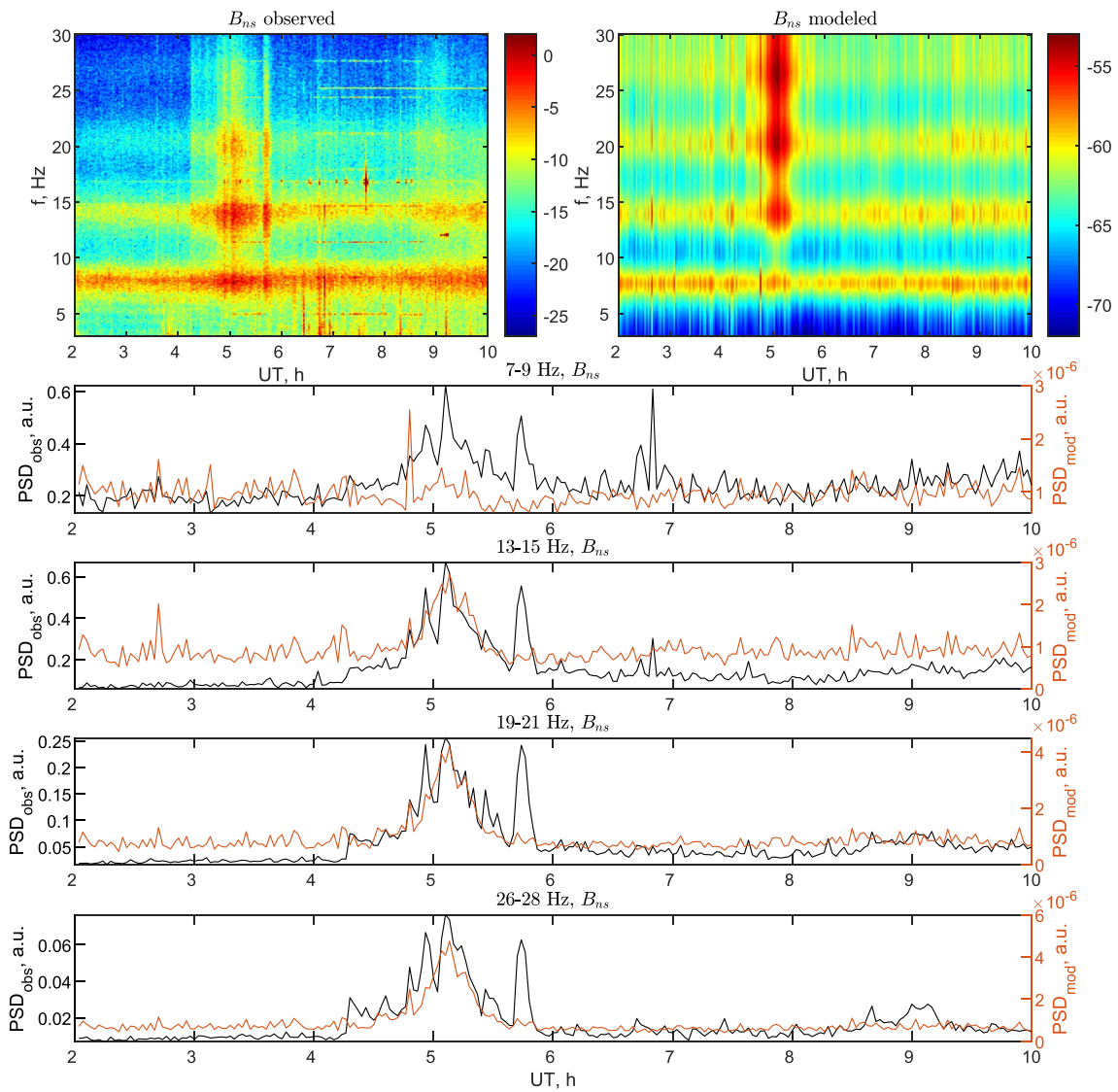


**Figure 15.** Power spectral density (PSD) spectrograms and averaged PSD along first four Schumann resonance peaks for Lot et Garonne (GRN) station for observed and modeled NS magnetic field component.

Thus, observed spectra from stations KRM, NKG, FCH, and MST will be presented for  $B_{\varphi_0}$  and  $B_{r_0}$  magnetic field components, see Equations 3; modeled spectra are constructed for  $H_{\varphi_0}$  and  $H_{r_0}$  magnetic field components, by use of Equations 4 and 2. CMN PSDs will be presented for vertical electric field  $E_z$ , see Equations 5 and 1. And GRN station will be shown as PSDs of  $B_{ns}$  and  $H_{ns}$ . Modeled PSD for  $H_{ns}$  can be evaluated (due to  $23^\circ$ E declination of the axis of GRN magnetometer) by using the second of Equations 4 with  $\alpha_0 = (90 + 23)^\circ$ :

$$H_{ns}^2 = H_{\varphi_0}^2 |_{\alpha_0=(90+23)^\circ}. \quad (6)$$

All spectrograms are constructed with PSDs calculated on 10 s non-overlapping time intervals (to keep the same frequency resolution for each station), which were then averaged over 2 min window. Spectrograms are shown in dB units:

$$C = 10 \lg \left( \frac{|X_a|^2}{T} \right). \quad (7)$$

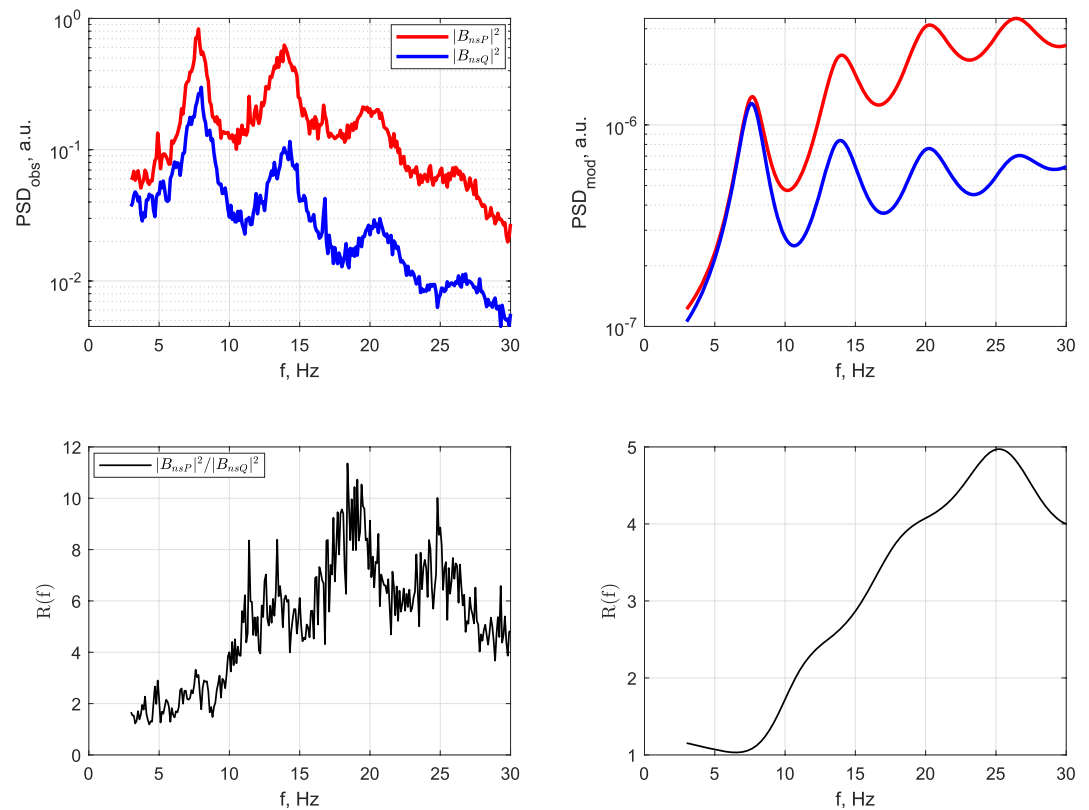


**Figure 16.** Characteristics of Schumann resonance power spectral density for observed and modeled data during eruption (04:50–05:10 UT) and quiet periods (03:02–03:22 UT) at Lot et Garonne observatory.

where  $C$  is PSD in dB,  $X_a$  is amplitude spectral density of desired field component,  $T$  is considered time interval (in our case it is always 10 s). All stations except for FCH and MST are shown within frequency range 3–30 Hz. Stations FCH and MST, due to their low sampling frequency are only presented within 5–10 Hz (band below 5 Hz is polluted by strong local noise).

Integrating spectrograms over frequency intervals of four first SR peaks (7–9, 13–15, 19–21, and 26–28 Hz) we can analyze observed and modeled SR spectra in more detail. We calculate those integral curves for all stations and all presented field components, based both on observed and modeled data. These curves show the power distribution between SR peaks for different field components at different geographical locations relative to the source of emission (Tonga volcano). Two stations, FCH and MST have integral curves for the first SR peak only due to their limited frequency range.

To analyze power distribution over frequency band, we also integrate the spectrograms over two 20 min time periods: during the peak of Tonga related lightning activity, 04:50 to 05:10 UT, and during a quiet period before the eruption. We chose these quiet periods to be slightly different for different stations, in order to avoid contamination from local nearby thunderstorms. These spectral curves allow for detailed comparison between observed and modeled results. In both cases after integration we normalize produced integral curves by the integration interval, which turns those curves to be average power per unit time or unit frequency correspondingly, so that we can easily relate those curves with spectrogram values.

### 5.1. Karimshino Observatory, KRM

Figure 7 shows PSD spectrograms of transversal  $B_\phi$  and longitudinal  $B_z$  horizontal magnetic field components, observed (left two panels) and modeled (right two panels) at KRM station. Color bar shows PSD values in dB. Four first SR peaks can be clearly distinguished at each spectrogram. We can see that SR enhancements during Tonga eruption only survive in transversal magnetic field component  $B_\phi$  and disappear in longitudinal component

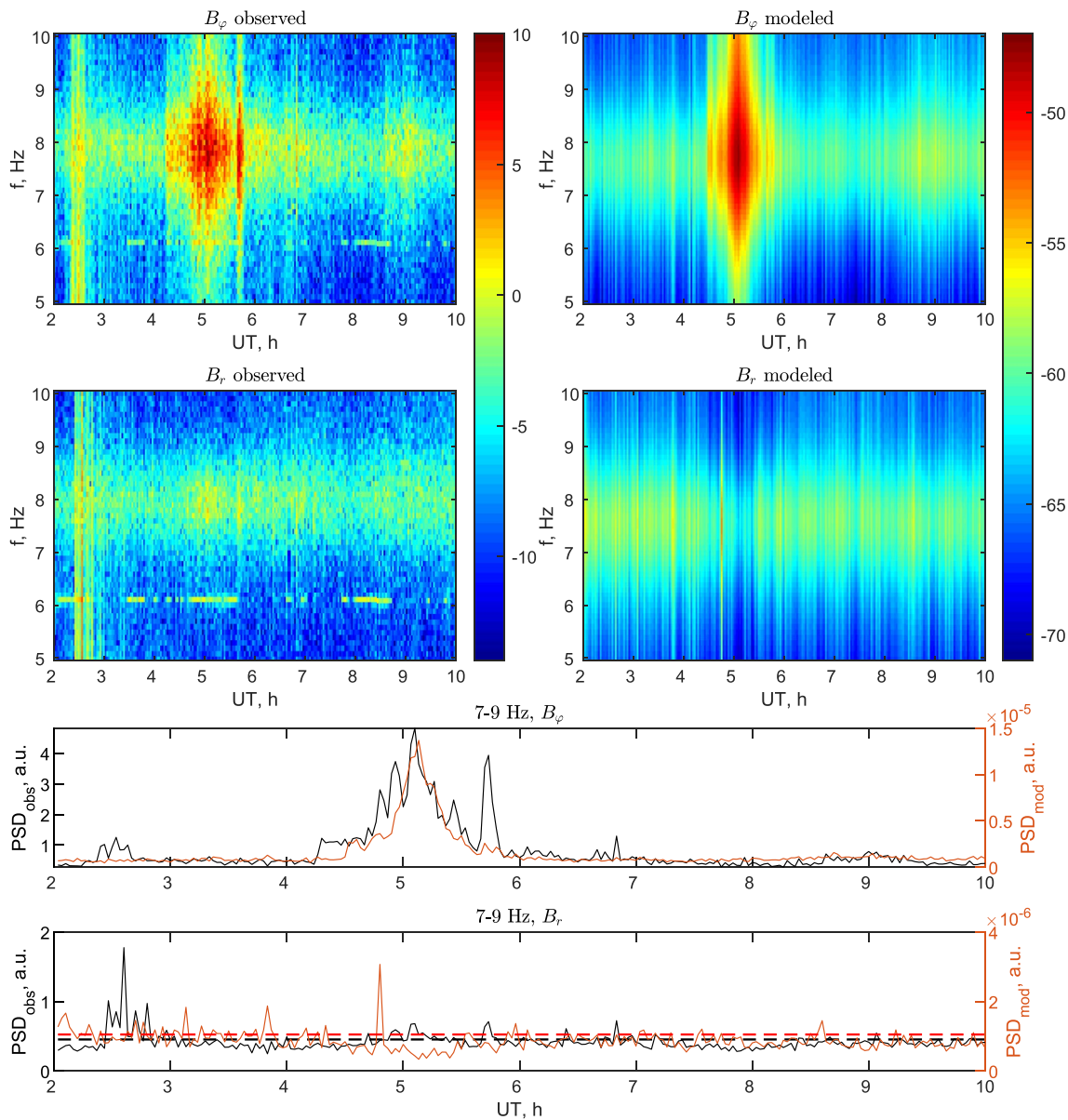


**Figure 17.** Power spectral density (PSD) spectrograms and averaged PSD along first Schumann resonance peak for FCH station for observed and modeled transversal and longitudinal components of magnetic field.

$B_r$ . This fact confirms that those SR enhancements indeed originate from ELF radiation coming from lightning sources around Tonga volcano. This is remarkable, and this relation between magnetic field components stays valid for all observatories that monitor two horizontal magnetic field components.

We can infer another important conclusion from the spectrogram of observed longitudinal field component. SR intensities in observed  $B_r$  spectrogram do not experience any enhancement during active phase of Tonga eruption, and stay at the same level as before and after the eruption, and also coincide with SR intensities of observed  $B_\varphi$  component for quiet period before the eruption. These intensities represent global lightning activity. Unchanged levels of SR intensities at  $B_r$  component during the eruption clearly indicate that global lightning activity was not affected by Tonga eruption, contrary to significant decrease in WLLN global detection rate  $R_G$ . This fact proves that the origin of the dip in the global WLLN flash rate  $R_G$  is purely instrumental (see previous section).

Another remarkable thing is that the global flash rate  $R_G$  decrease is clearly seen in the modeled  $B_r$  spectrogram, based on WLLN recordings. This is totally expected: if global WLLN flash rate experiences significant

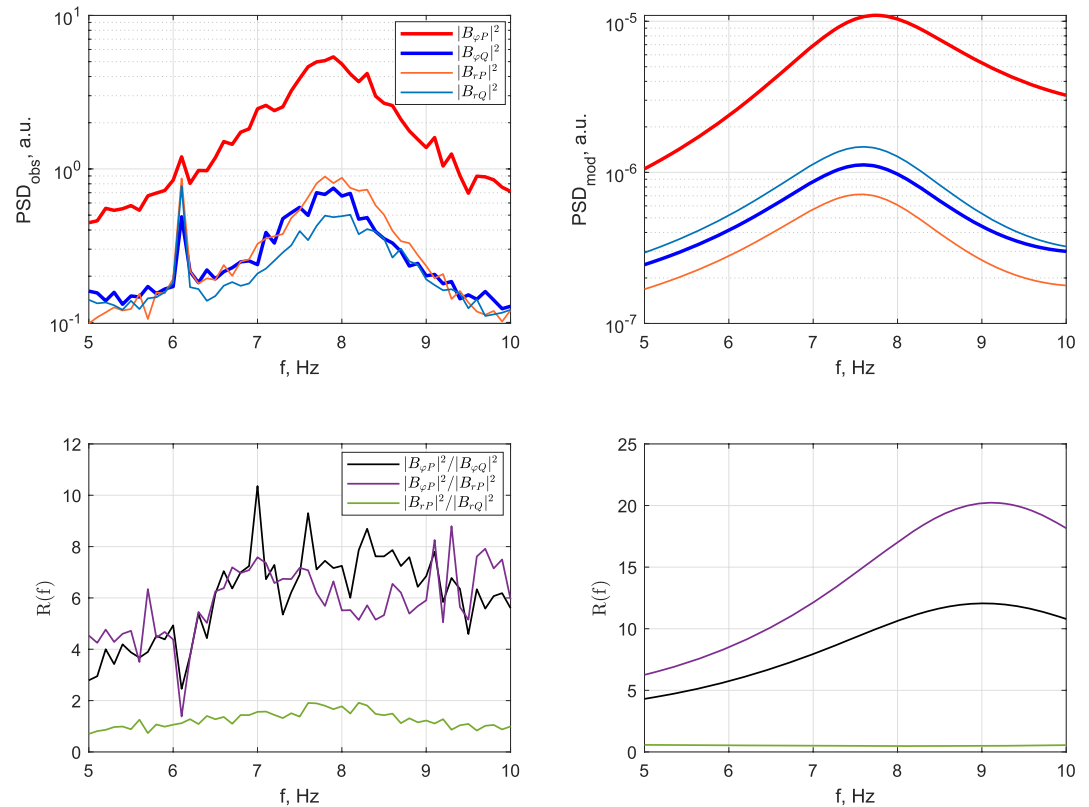


**Figure 18.** Characteristics of Schumann resonance power spectral density for observed and modeled data during eruption (04:50–05:10 UT) and quiet periods (03:32–03:52 UT) at FCH observatory.

decrease, this must be reflected in the modeled  $B_r$  spectra, which represent reported global lightning activity. Our results show exactly this: significant decrease in the modeled  $B_r$  spectrogram during the active phase of Tonga eruption.

Integrating Figure 7 spectrograms over frequency intervals of four first SR peaks (7–9, 13–15, 19–21, and 26–28 Hz) we can analyze observed and modeled SR spectra in more detail. Figure 8 shows comparisons between observed (black curves) and modeled (orange curves) intensities of four SR peaks for transversal magnetic field component  $B_\phi$  (upper panels) and longitudinal magnetic field component  $B_r$  (lower panels). Black and red dashed lines in right panels show average PSD levels of observed and modeled  $B_r$ , calculated based on the quiet time interval 02:00 to 04:00 UT. We can clearly see the dip in PSD levels of modeled  $B_r$  in all frequencies, which reflects the dip in global WWLLN detection rate during the active phase of Tonga eruption.

Left panels of Figure 8 characterize the signal from Tonga associated activity itself. We can see that the main peak of activity (around 05:00 UT) clearly coincides between observed and modeled spectra. However, observed curves have certain fine structure which correlates with lightning activity around Tonga (Figure 21), but is totally uncorrelated with the fine structure of the modeled curve (see discussion below).

Integrating spectrograms from Figure 7 over 20 min time period of peak Tonga activity (which we denote as “peak” period), 04:50 to 05:10 UT, and quiet 20 min time period, 03:40 to 04:00 UT, we can characterize power distribution over frequency range in different field components during peak and quiet periods. Figure 9 presents those integral spectral curves. Left and right panels show observed and modeled data correspondingly. Upper panels show  $B_\phi$  PSD during peak period, which represents total Tonga related signal (red curve);  $B_\phi$  PSD during quiet period, which could serve as a reference level in signal channel (blue curve);  $B_r$  PSD during peak period, which should not contain signal from Tonga and could serve as a reference channel during peak power of Tonga signal (orange curve); and  $B_r$  PSD for quiet period, which can also be used as a reference level in reference channel (cyan curve).



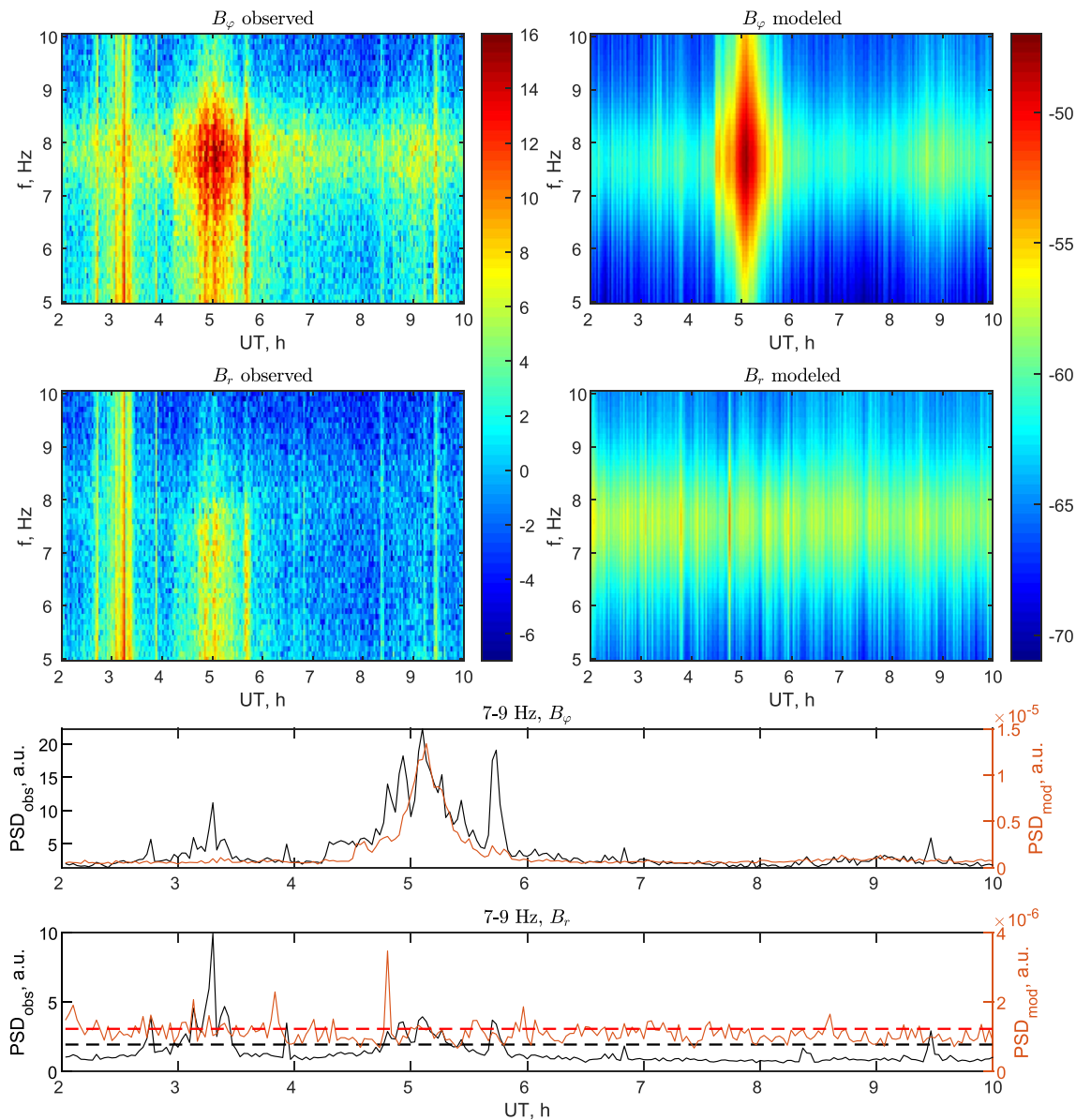


**Figure 19.** Power spectral density (PSD) spectrograms and averaged PSD along first Schumann resonance peak for MST station for observed and modeled transversal and longitudinal components of magnetic field.

Lower panels characterize relative power increase:  $B_\phi$  during peak over quiet period (signal power increase in the signal channel over its own reference level, black curve);  $B_\phi$  over  $B_r$  during peak period (signal power increase in the signal channel over the reference channel during peak period, purple curve);  $B_r$  during peak over quiet period (characterizes power increase in the reference channel during peak period over quiet period, green curve).

From upper panels of Figure 9 we can see that spectral structure of the signal in the model is very close to the observed one (red curves on the right and left upper panels). Also we can see that all three reference curves stay close to each other for the observed data (left panel). Note that orange curve in the right panel drops down by about a factor of 2 compared to other reference curves. This is related to the significant decrease in global WWLLN detection rate  $R_G$  that we discussed in the previous section. Also note that the orange curve in the left panel does not show any decreasing tendency compared to the other reference curves. This confirms the fact that real global lightning activity was not affected anyhow by Tonga eruption, and the dip in WWLLN detection efficiency during Tonga eruption was instrumental.

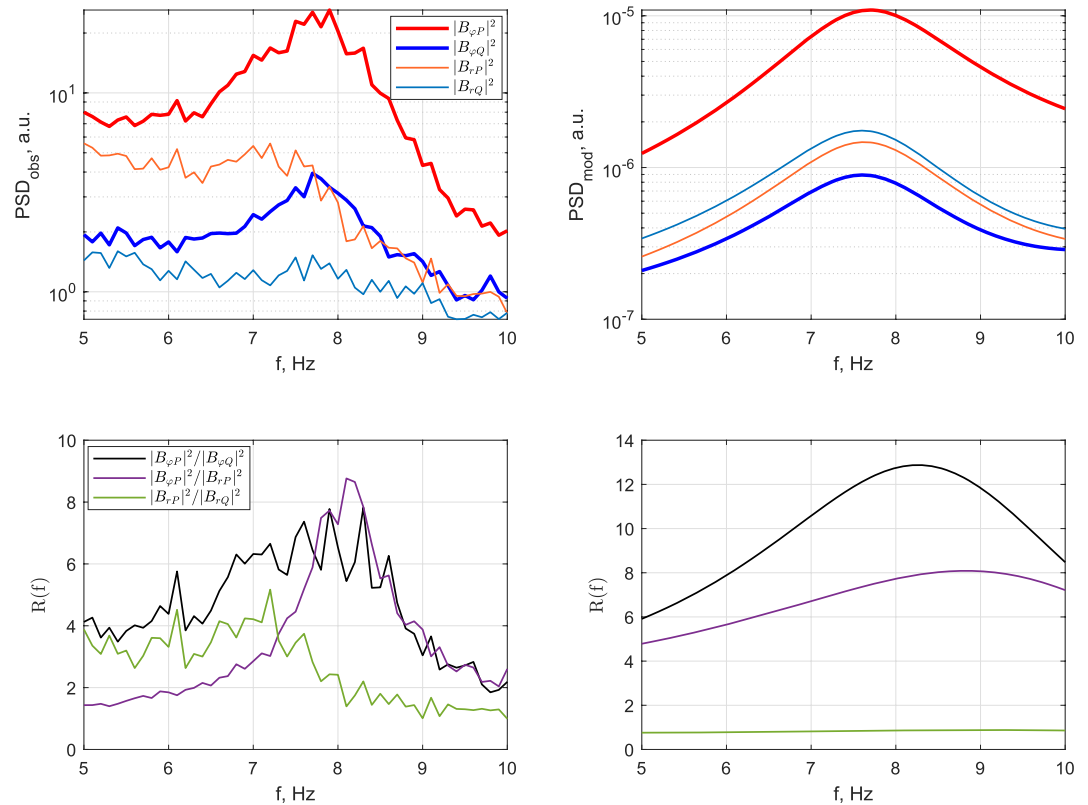


**Figure 20.** Characteristics of Schumann resonance power spectral density for observed and modeled data during eruption (04:50–05:10 UT) and quiet periods (03:32–03:52 UT) at MST observatory.

Lower panels of Figure 9 characterize frequency dependence of power enhancement during the peak period. We can also infer some conclusions about the source of emission and the station itself. We can see that in the left lower panel black and purple curves are pretty close to each other. This indicates that the source of emission was very compact, nearly a point source (which we know from lightning distribution around Tonga, see Figure 2), and the magnetometer coils for  $B_{ns}$  and  $B_{ew}$  were properly oriented. Excess of the purple curve over the black curve in the right lower panel indicates again the dip in WWLLN detection efficiency during Tonga eruption. Green curves on both panels characterize “goodness” of the reference channel: if the station magnetometers were properly oriented, the source was compact, and other sources did not contribute much, then the green curves should be close to the value of 1. This is exactly what we see in both panels, which shows the high quality of KRM station.

## 5.2. Nakatsugawa Observatory, NKG

Figure 10 shows PSD spectrograms of observed and modeled  $B_\phi$  and  $B_r$  components, calculated for NKG station. We can see a high level of local pulsed EM noise at NKG site, which looks like a contribution from a nearby local thunderstorm.

In Figure 11 we see a similar result to KRM station, with dip in modeled  $B_r$  curves during the peak of Tonga eruption, which is due to decrease of WWLLN detection efficiency during that period. However, we can point out one peculiar difference between KRM and NKG results. Comparing left panels of Figures 8 and 11 we can see that at KRM site the level of EM noise from nearby thunderstorms was quite low (no spikes on the black curves in Figure 8, left panels), whereas modeled curves (and spectrograms) show very noisy environment: noise level, especially for higher SR peaks is comparable with the level of signal from Tonga (lots of high amplitude spikes on the orange curves in Figure 8, left panels). This feels counter intuitive and should be explained somehow.

At the same time there is quite the opposite picture for NKG station. Indeed, the local noise level is quite high, which can be seen from spectrograms and by the spikes on black curves in Figure 11, left panels. But modeled

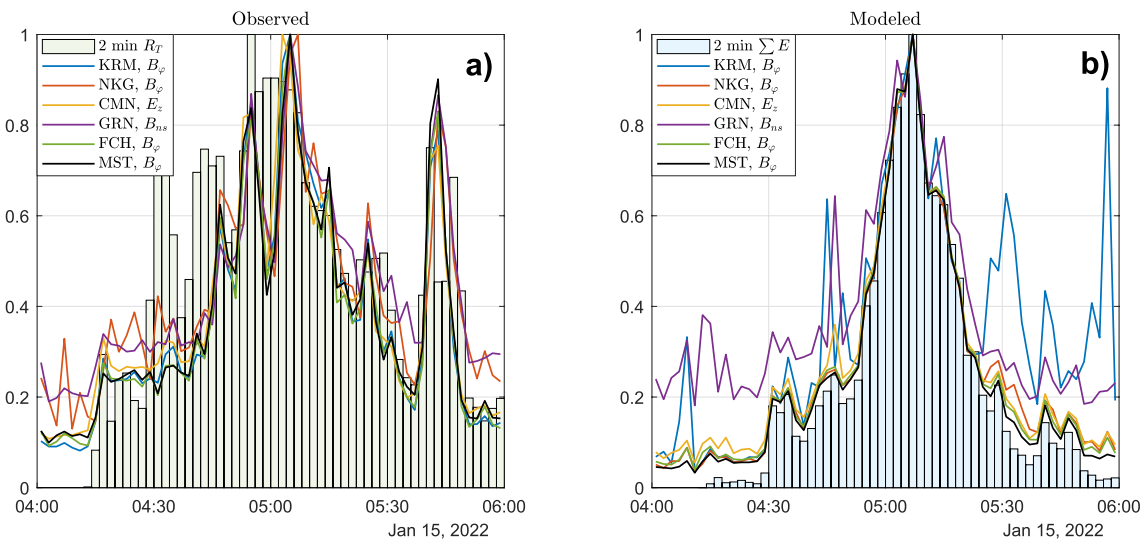


**Figure 21.** Comparison between frequency integrated spectrograms for observed and modeled data with Tonga associated World Wide Lightning Location Network lightning flash rate  $R_T$  (a) and energy release (b). All integral curves are normalized to 1. Lightning flash rate and energy release (shown as histograms) are also normalized to 1. Stations KRM, NKG, FCH, MST are presented by  $B_\phi$  power spectral density integrated over frequency. CMN station is shown by  $E_z$ , and GRN station is presented by  $B_{ns}$  integral curve. All stations spectrograms are integrated over 3–30 Hz frequency range, except for FCH and MST stations, which are integrated over 5–10 Hz interval.

curves do not show any sign of noisy environment (orange curves are smooth in Figure 11, left panels). This is even more counter intuitive than for KRM station. Partially these two strange things could be explained by the decreased detection efficiency of WWLLN during active phase of Tonga eruption, which leads to underestimation of the energy release by Tonga lightning discharges. Partially the difference in local EM noise level at KRM and NKG stations could be explained by significantly different azimuth from local thunderstorm toward KRM and NKG. However, we have not investigated this difference in detail yet.

Spectral curves, characterizing power emission during peak and quiet periods are shown in Figure 12. From the upper left panel, which shows observed results, we can conclude that the amplitude frequency response of the NKG induction coil magnetometers decreases with frequency within 3–30 Hz range. Accounting for this decreasing amplitude frequency response, we can see that the spectral emission patterns are nearly identical between observed and modeled signal emissions in signal channel. Orange curve in the right upper panel is at about factor of 2 lower level compared to the cyan curve (see previous subsection where we discuss this in detail), which is expected due to decreased WWLLN detection efficiency during the eruption. The blue curve in both upper panels is significantly lower than other reference curves, which is due to strong contribution of the local thunderstorm. The green curves at the lower panels are sitting at the level of 1, which shows that magnetometer coils were properly oriented. The spectral pattern of Tonga signal is quite similar to the result at KRM observatory. These two stations have similar distance and azimuth toward Tonga volcano, which explains similarity in the results.

### 5.3. Cumiana Observatory, CMN

Spectrograms and integral curves for CMN observatory are presented in Figure 13. Here only vertical electric field component  $E_z$  is monitored. The main peak of Tonga activity is clearly seen in the modeled data (orange curves in graph panels in Figure 13). Also it is clearly seen that neither activity during quiet periods, nor characteristic pattern of activity during the eruption in modeled data are correlated with the observed results. Several periods of extremely strong surges of local lightning activity in the observed data passed totally unnoticed in the modeled data. Although the spectral pattern of power emission for the main Tonga signal in modeled data is very close to the observed one (see Figure 14).

### 5.4. Lot et Garonne Observatory, GRN

Figure 15 shows spectrograms and integral curves for GRN station, which only monitors one magnetic field component  $B_{ns}$ . Here we can say again that any fine structure in the local activity or any pattern in the Tonga

signal, apart from the main peak, cannot be reproduced by the model. All local activity in the real data looks totally uncorrelated with the modeled data.

From Figure 16, upper panels, we can conclude that the amplitude frequency response decreases with frequency for GRN magnetometer. If we take this into account, then we can say that spectral power emission pattern for Tonga signal nicely correlates between model and observations.

### 5.5. CARISMA FCHU Observatory, FCH

FCH station records both horizontal magnetic field components, but public data are available with 20 Hz sampling frequency. Thus, Figure 17 shows spectrograms for observed (left panels) and modeled (right panels) transversal  $B_\phi$  (upper panels) and longitudinal  $B_r$  (lower panels) magnetic field components. Two bottom panels show integral curves for the first SR peak. We can see again that the fine structure of Tonga signal cannot be reproduced by the model. Modeled  $B_r$  integral curve (this also seen in the modeled  $B_r$  spectrogram) has a dip during Tonga eruption, which is due to decrease of WWLLN detection efficiency.

Spectral curves in Figure 18 show similar pattern, however, it is hard to say how reliable this similarity is, because only first SR peak is presented. However, the green curves in lower panels are close to the value of 1, which shows that magnetometer coils were properly oriented.

### 5.6. CARISMA MSTK Observatory, MST

Figure 19 shows the same results for MST station, as Figure 17 for FCH station: these two observatories are quite similar and belong to the same CARISMA network. From the spectrogram for observed  $B_r$  (lower left) we can see that Tonga signal did not disappear (as it should), and its level constitutes about 20% of the level in  $B_\phi$ . We can see this problem even more clear in Figure 20: the green curve in the lower left panel is very far from being at the level of 1. This can be the result of either not precise orientation of the magnetometer coils along NS and EW directions, or incorrectly reported relative amplitudes of the coils.

## 6. Discussion

We have shown in the presented results that lightning activity associated with Tonga volcano produced significant enhancements in SR worldwide. These enhancements by the power level reach values of 8–12 (see black curves in lower left panels in Figures 9, 12, 14, 16, 18, and 20). This means that Tonga associated lightning activity for the peak hour was emitting 10 times more power than the whole planet. This is absolutely unprecedented in the history of EM observations.

We have also demonstrated that our model of ELF propagation in the Earth-ionosphere waveguide with WWLLN detections as a field source produce reliable results, which gives similar spectral power emission patterns for globally separated stations, for different EM field components. However, we have to admit that only peak of maximal energy release in the modeled data correlates well with the observed data. Neither fine time structure of the Tonga signal, nor local thunderstorm disturbances, sometimes very strong, could be reproduced by our model.

We suggest that one of the main factors that affected accuracy of our model is that VLF lightning representation is in fact a pretty poor model of the ELF lightning representation. WWLLN is a VLF system, and SR model requires ELF field sources. We have also shown that unprecedentedly high flash rate above the volcano during its peak phase led to significant decrease of WWLLN detection efficiency. So, we cannot hope that during the eruption WWLLN was giving somehow correct picture of global lightning activity, nor correct representation of Tonga associated activity. Although Tonga associated activity was so high, that even significantly distorted, it could produce correct general results with our model.

We have mentioned several times that only main peak of Tonga related activity captured by model correlates well with the observations. The reason for that is quite obvious. Figure 21 shows integral curves for all 6 stations (signal containing field component spectrograms integrated over frequency) for observed (left panel) and modeled (right panel) data. It is obvious that the curves nicely correlate between different stations within certain representation (observed or modeled), but are totally uncorrelated between the two representations (except for the main peak).

In addition, we have plotted Tonga associated WWLLN flash rate over observed curves (left panel). Here we can see a certain correlation, although far from perfect. But the main peak of the flash rate, and the second main peak at 05:36 to 05:50 UT (highlighted with red in Figures 3b and 3c) correlate perfectly with the first and second main peaks of the SR enhancements. Modeled results could never reproduce the second main peak. The reason for that is the assumption about source current moment being proportional to the square root of WWLLN reported stroke energy. This assumption (see Equations 1 and 2) makes the PSD of geographically compact sources proportional to the released energy. In the right panel of Figure 21 we have plotted the histogram of the total energy release reported by WWLLN from Tonga associated lightning discharges. We can see that this energy release perfectly correlates with the modeled integral curves, even in minor detail (with some disturbance from local noise for KRM station).

From our results we can conclude that we need a better representation of global lightning activity in ELF frequency range, and that WWLLN, being a VLF system, cannot provide such representation. WWLLN can be used when EM source is geographically compact, and the energy release of this source exceeds the whole planetary activity by an order of magnitude.

## 7. Conclusion

We have presented observed and modeled results of the impact of Tonga volcano eruption (15 January 2022) on global SR, recorded at six globally separated stations. We have used our model of the ELF radio wave propagation in the Earth-ionosphere waveguide, equipped with WWLLN lightning data as a field source, with some simplifying assumptions (average day-night conductivity profile, VLF lightning representation instead of ELF representation, usage of reported stroke energy as a square of the current moment, Poissonian character of WWLLN detections).

Despite of those quite strong assumptions, some of which could never be correct, we managed to demonstrate that modeled results agree quite well with the observations. We have shown that general peak of SR enhancement coincides nicely with the reported data. Modeled increase levels of power emissions in SR frequencies correspond to those of the observed data. Spectral power emission patterns also coincide for different geographical locations and different field components.

This shows the reliability of our propagation model in the Earth-ionosphere waveguide. However, detailed discrepancies show that WWLLN representation of detected lightning activity cannot be used in ELF frequency range.

We have also demonstrated that during Tonga eruption WWLLN experienced significant distance dependent decrease in its detection efficiency, due to extraordinarily high lightning flash rate associated with Tonga eruption. It would be very helpful if WWLLN operating team would include actual values of trigger threshold in their distribution lists, as those trigger thresholds characterize the global WWLLN detection efficiency, and at the current moment this information is not provided.

## Data Availability Statement

The data, the model and its usage, described in this study are uploaded to Zenodo and can be found and downloaded from here: <https://doi.org/10.5281/zenodo.7068451> (Mezentsev et al., 2022).

## References

- Astafyeva, E., Maletkii, B., Mikesell, T. D., Munaibari, E., Ravanelli, M., Coisson, P., et al. (2022). The 15 January 2022 Hunga Tonga eruption history as inferred from ionospheric observations. *Geophysical Research Letters*, 49(10). <https://doi.org/10.1029/2022GL098827>
- Burke, C. P., & Jones, D. L. (1996). On the polarity and continuing currents in unusually large lightning flashes deduced from ELF events. *Journal of Atmospheric and Terrestrial Physics*, 58(5), 531–540. [https://doi.org/10.1016/0021-9169\(95\)00054-2](https://doi.org/10.1016/0021-9169(95)00054-2)
- Füllekrug, M. (2021). Simulation of Earth-ionosphere cavity resonances with lightning flashes reported by OTD/LIS. *Journal of Geophysical Research: Atmospheres*, 126(24). <https://doi.org/10.1029/2021JD035721>
- Galuk, Y. P. (2016). Schumann resonance in the model of thunderstorm activity uniformly distributed over the globe. *Telecommunications and Radio Engineering*, 75(10), 923–935. <https://doi.org/10.1615/TelecomRadEng.v75.i10.60>
- Hutchins, M. L., Holzworth, R. H., Brundell, J. B., & Rodger, C. J. (2012). Relative detection efficiency of the World Wide Lightning Location Network. *Radio Science*, 47(6), RS6005. <https://doi.org/10.1029/2012RS005049>
- Jacobson, A. R., Holzworth, R., Harlin, J., Dowden, R., & Lay, E. (2006). Performance Assessment of the World Wide Lightning Location Network (WWLLN), using the Los Alamos Sferic Array (LASA) as Ground Truth. *Journal of Atmospheric and Oceanic Technology*, 23(8), 1082–1092. <https://doi.org/10.1175/JTECH1902.1>

## Acknowledgments

The authors thank I. R. Mann, D. K. Milling and the rest of the CARISMA team for data. CARISMA is operated by the University of Alberta, funded by the Canadian Space Agency. The authors are most grateful to Jean Marie Briussel and Michel Brunel for their efforts in monitoring the natural ULF/ELF radio signals at the Lot et Garonne station. The authors wish to thank the World Wide Lightning Location Network (<http://wwlln.net>), a collaboration among over 50 universities and institutions, for providing the lightning location data used in this paper. Contributions of APN and AVS are in the framework of their departmental research work “Iveria” (#0122U000585). AVS is grateful to the Nippon Foundation, the University of Electro-Communications and prof. Yasuhide Hobara for their support of his stay and opportunity to continue his work in Japan. Contribution of AM was supported by Research Council of Norway under contracts 223252/F50 (CoE). Also AM wants to personally thank Martin Füllekrug and Jone Reistad for useful and fruitful discussions.



- Jones, D. L. (1976). Schumann resonances and E.L.F. propagation for inhomogeneous isotropic ionospheric profiles. *Journal of Atmospheric and Terrestrial Physics*, 29(9), 1037–1044. [https://doi.org/10.1016/0021-9169\(67\)90138-9](https://doi.org/10.1016/0021-9169(67)90138-9)
- Kudintseva, I. G., Nickolaenko, A. P., Rycroft, M. J., & Odzimek, A. (2016). AC and DC global electric circuit properties and the height profile of atmospheric conductivity. *Annals of Geophysics*, 59(5), A0545. <https://doi.org/10.4401/ag-6870>
- Kudintseva, I. G., Nikolayenko, S. A., Nikolaenko, A. P., & Hayakawa, M. (2017a). Schumann resonance background signal synthesized in time. *Telecommunications and Radio Engineering*, 76(9), 807–826. <https://doi.org/10.1615/telecomradeng.v76.i9.60>
- Kudintseva, I. G., Nikolayenko, S. A., Nikolaenko, A. P., & Hayakawa, M. (2017b). Synthesis of Schumann resonance background signal in time domain. *International Journal of Electronics and Applied Research*, 4(1), 1–23. Retrieved from <http://eses.net.in/documents/paper4.1.1.pdf>
- Mann, I. R., Milling, D. K., Rae, I. J., Ozeke, L. G., Kale, A., Kale, Z. C., et al. (2008). The upgraded CARISMA magnetometer array in the THEMIS Era. *Space Science Reviews*, 141(1–4), 413–451. <https://doi.org/10.1007/s11214-008-9457-6>
- Matoza, R. S., Fee, D., Assink, J. D., Iezzi, A. M., Green, D. N., Kim, K., et al. (2022). Atmospheric waves and global seismoacoustic observations of the January 2022 Hunga eruption, Tonga. *Science*, 377(6601), 95–100. <https://doi.org/10.1126/science.abo7063>
- Mezentsev, A., Nikolaenko, A. P., Shvets, A. V., & Galuk, Y. P. (2022). Data, software and supporting information for “observational and model impact of Tonga volcano eruption on Schumann resonance”. [Dataset]. Zenodo. <https://doi.org/10.5281/zenodo.7068451>
- Nickolaenko, A. P., Galuk, Y. P., & Hayakawa, M. (2016). Vertical profile of atmospheric conductivity that matches Schumann resonance observations. *SpringerPlus*, 5(108). <https://doi.org/10.1186/s40064-016-1742-3>
- Nickolaenko, A. P., & Hayakawa, M. (2002). *Resonances in the Earth-ionosphere cavity*. Springer.
- Nickolaenko, A. P., & Hayakawa, M. (2014). *Schumann resonance for Tyros*. Springer Tokyo. <https://doi.org/10.1007/978-4-431-54358-9>
- Nickolaenko, A. P., Schekotov, A. Y., Hayakawa, M., Romero, R., & Izutsu, J. (2022). Electromagnetic manifestations of Tonga eruption in Schumann resonance band. *Journal of Atmospheric and Solar-Terrestrial Physics*, 237, 105897. <https://doi.org/10.1016/j.jastp.2022.105897>
- Nickolaenko, A. P., Shvets, A. V., & Hayakawa, M. (2016a). Extremely low frequency (ELF) radio wave propagation: A review. *International Journal of Electronics and Applied Research*, 3(2), 91. Retrieved from <http://eses.net.in/documents/paper3.2.1.pdf>
- Nickolaenko, A. P., Shvets, A. V., & Hayakawa, M. (2016b). Propagation of extremely low-frequency radio waves. In J. Webster (Ed.), *Wiley encyclopedia of electrical and electronics engineering* (pp. 1–20). John Wiley & Sons, Inc. <https://doi.org/10.1002/047134608X.W1257.pub2>
- Rodger, C. J., Brundell, J. B., & Dowden, R. L. (2005). Location accuracy of VLF World-Wide Lightning Location (WWLL) network: Post-algorithm upgrade. *Annales Geophysicae*, 23(2), 277–290. <https://doi.org/10.5194/angeo-23-277-2005>
- Rodger, C. J., Brundell, J. B., Dowden, R. L., & Thomson, N. R. (2004). Location accuracy of long distance VLF lightning location network. *Annales Geophysicae*, 22(3), 747–758. <https://doi.org/10.5194/angeo-22-747-2004>
- Shvets, A. V., Hobar, Y., & Hayakawa, M. (2010). Variations of the global lightning distribution revealed from three-station Schumann resonance measurements. *Journal of Geophysical Research*, 115(A12), A12316. <https://doi.org/10.1029/2010JA015851>
- Shvets, A. V. (2001). A technique for reconstruction of global lightning distance profile from background Schumann resonance signal. *Journal of Atmospheric and Solar-Terrestrial Physics*, 63(10), 1061–1074. [https://doi.org/10.1016/S1364-6826\(01\)00024-4](https://doi.org/10.1016/S1364-6826(01)00024-4)
- Wright, C. J., Hindley, N. P., Alexander, M. J., Barlow, M., Hoffmann, L., Mitchell, C. N., et al. (2022). Surface-to-space atmospheric waves from Hunga Tonga-Hunga Ha’apai eruption. *Nature*, 609(7928), 741–746. <https://doi.org/10.1038/s41586-022-05012-5>